© 2018. Published by The Company of Biologists Ltd | Development (2018) 145, dev158519. doi:10.1242/dev.158519

RESEARCH ARTICLE

Microtubule organization in presynaptic boutons relies on the formin DAAM

Ede Migh[1], Torsten Götz[2], István Földi[1], Szilárd Szikora[1], Rita Gombos[1], Zsuzsanna Darula[3], Katalin F. Medzihradszky[3], József Maléth[4], Péter Hegyi[4,5], Stephan Sigrist[2] and József Mihály[1,*]

ABSTRACT

Regulation of the cytoskeleton is fundamental to the development and function of synaptic terminals, such as neuromuscular junctions. Despite the identification of numerous proteins that regulate synaptic actin and microtubule dynamics, the mechanisms of cytoskeletal control during terminal arbor formation have remained largely elusive. Here, we show that DAAM, a member of the formin family of cytoskeleton organizing factors, is an important presynaptic regulator of neuromuscular junction development in *Drosophila*. We demonstrate that the actin filament assembly activity of DAAM plays a negligible role in terminal formation; rather, DAAM is necessary for synaptic microtubule organization. Genetic interaction studies consistently link DAAM with the Wg/Ank2/Futsch module of microtubule regulation and bouton formation. Finally, we provide evidence that DAAM is tightly associated with the synaptic active zone scaffold, and electrophysiological data point to a role in the modulation of synaptic vesicle release. Based on these results, we propose that DAAM is an important cytoskeletal effector element of the Wg/Ank2 pathway involved in the determination of basic synaptic structures, and, additionally, that DAAM may couple the active zone scaffold to the presynaptic cytoskeleton.

KEY WORDS: Formin, dDAAM, NMJ, Bouton formation, Microtubule, *Drosophila*

INTRODUCTION

Elucidating the mechanisms of synapse development and function is crucial to understanding fundamental neuronal processes such as learning and memory and, consequently, a broad spectrum of neurological diseases. Research over the past few decades has established that proper regulation of cytoskeletal dynamics is essential for the development, maintenance, plasticity and functioning of synaptic terminals. The actin cytoskeleton is involved in presynaptic terminal formation, synaptic vesicle (SV) release, synaptic active zone (AZ) formation, dendritic arbor assembly and spine plasticity (reviewed by Bosch and Hayashi, 2012; Cingolani and Goda, 2008; Nelson et al., 2013). Similarly, the microtubule (MT) cytoskeleton was shown to play a role in the regulation of neurotransmitter release, AZ density, dendritic spine morphology, and in synapse remodeling and plasticity (Goellner and Aberle, 2012; Kevenaar and Hoogenraad, 2015; Nelson et al., 2013). Furthermore, an actin/spectrin/ankyrin/MT cortical membrane skeleton has been distinguished as an important determinant of synapse organization and stability (Goellner and Aberle, 2012; Pielage et al., 2005, 2008).

Mutational analysis in model organisms has been used to identify the cytoskeletal regulatory proteins employed during synapse development. Studies in *Drosophila* neuromuscular junctions (NMJs), for instance, have been particularly informative in deciphering the role of the MAP1B homolog Futsch in synaptic MT stabilization (Hummel et al., 2000; Roos et al., 2000), in the regulation of AZ number and SV release (Lepicard et al., 2014), and in activity-dependent AZ remodeling (Sugie et al., 2015). Other studies have revealed that a spectrin and Ankyrin 2 (Ank2)-dependent cortical scaffold is essential for synapse maintenance (Koch et al., 2008; Pielage et al., 2005, 2008). It has also been shown that Ank2 proteins act in concert with Futsch to regulate synaptic MT organization and stability (Koch et al., 2008; Pielage et al., 2008; Stephan et al., 2015) under the control of Wnt-Frizzled signaling (Luchtenborg et al., 2014) and casein kinase 2 (CK2)-dependent phosphorylation (Bulat et al., 2014). In addition to MTs, actin is also highly concentrated at synapses, and findings in *Drosophila* indicate that F-actin assembly is crucial for presynaptic bouton formation and terminal arborization (Koch et al., 2014), whereas local F-actin rearrangements are important for recruitment and assembly of AZs in *C. elegans* (Chia et al., 2012, 2014). Despite these advances, the molecular mechanisms of neuroskeletal regulation in synaptic areas has remained largely elusive.

Formins are highly conserved cytoskeleton modulatory proteins with well-characterized roles in actin filament assembly and functions in MT organization and stabilization (Chesarone et al., 2010). Owing to their ability to bind both cytoskeletal components directly and to interact with MT plus-end-binding proteins, formins were recently linked to actin-MT crosstalk in both neurons (Henty-Ridilla et al., 2016; Szikora et al., 2017) and non-neuronal cells (Bartolini et al., 2008; Chesarone et al., 2010; Gaillard et al., 2011; Rosales-Nieves et al., 2006; Young and Copeland, 2010). Interestingly, Diaphanous (Dia), the founding member of the Diaphanous-related formin (DRF) family, is known to be required for synaptic growth in *Drosophila* NMJs (Pawson et al., 2008), where it has been implicated in presynaptic actin organization and regulation of a dynamic MT population. Members of the DRF family are thought to be regulated by an intramolecular autoinhibitory mechanism that can be relieved upon Rho GTPase binding (Chesarone et al., 2010); consistently, Dia appears to act downstream of the receptor protein tyrosine phosphatase Lar (also known as Dlar) and the RhoGEF *trio*. Thus, Dia-dependent Lar

[1]Institute of Genetics, Biological Research Centre, Hungarian Academy of Sciences, MTA-SZBK NAP B Axon Growth and Regeneration Group, Temesvári krt. 62, Szeged H-6726, Hungary. [2]Institut für Biologie/Genetik and NeuroCure, Freie Universitat Berlin, Takustrasse 6, D-14195 Berlin, Germany. [3]Laboratory of Proteomics Research, Biological Research Centre, Hungarian Academy of Sciences, Szeged H-6726, Hungary. [4]MTA-SZTE Translational Gastroenterology Research Group, Szeged H-6725, Hungary. [5]Institute for Translational Medicine, University of Pecs, Pécs H-7624, Hungary.

*Author for correspondence (mihaly.jozsef@brc.mta.hu)

J.M., 0000-0003-3399-2424

Received 14 August 2017; Accepted 14 February 2018

Development (2018) 145, dev158519. doi:10.1242/dev.158519

signaling appears to play an important role in synapse development, yet the cytoskeletal effectors of other signaling cascades involved in synapse formation and function have remained unidentified.

We show here that mutations in *Dishevelled associated activator of morphogenesis* (*DAAM*; also known as *dDAAM*), another member of the DRF family, impairs synaptic bouton formation in *Drosophila* NMJs. Although DAAM protein accumulates at both the presynaptic and postsynaptic faces of the NMJ, genetic analysis primarily supports a role in presynaptic development. Despite formins being best known for their ability to promote F-actin assembly, we provide evidence that DAAM is necessary for MT organization and stabilization in developing synaptic boutons. Our genetic interaction studies indicate that DAAM acts together with Wingless (Wg) and Ank2 during synapse development and might link cortical membrane skeleton regulation to organization of the central MT network. Remarkably, beyond the role in bouton formation, we revealed that DAAM is highly enriched at the synaptic scaffolds organized by the Bruchpilot (Brp) protein, where it appears to contribute to the modulation of synaptic transmission. Thus, the analysis of DAAM might help not only to elucidate the complex mechanisms of cytoskeletal regulation during presynaptic development, but also to open up new avenues for further exploration of the roles of cytoskeletal organization in SV release at AZs.

RESULTS

The formin protein DAAM is enriched in motoneuron terminals

Our previous studies demonstrated that DAAM plays a role in axonal growth and guidance in the *Drosophila* central nervous system (CNS) (Matusek et al., 2008), including the adult brain where the protein is present throughout the entire neuropile region (Gombos et al., 2015). We carried out affinity chromatography to identify potential novel interaction partners of DAAM to further explore its function during CNS development. We created a C-terminally 3×FLAG-tagged *DAAM* knock-in allele ($DAAM^{3xFlag}$) to avoid potential unwanted effects due to overexpression. This allele is fully viable in homozygous and hemizygous form, and the levels of the fusion protein were nearly equal to wild-type (WT) levels (Fig. S1A), indicating that DAAM::3×Flag is a functionally active protein, and the $DAAM^{3xFlag}$ allele is suitable for affinity purification. This experiment was carried out using adult heads of $DAAM^{3xFlag}$ flies, using a WT strain as a control for non-specific binding (Fig. S1B). Proteins eluted from the anti-Flag beads were subjected to an LC-MS/MS analysis. DAAM co-purified with a number of proteins, including Futsch, Ank2, Shaggy (Sgg; *Drosophila* GSK3β) and FMR1 (Fig. S1C), which are known to be active during synaptogenesis and involved in synapse function.

To address whether DAAM might be involved in synapse development, *Drosophila* NMJs were used as our principal synaptic model system. First, we examined the expression pattern of DAAM during synapse development from the embryonic to the larval stages. The embryonic motoneurons were visualized with Fasciclin 2 (FasII) staining in stage 15 embryos, where we found a strong overlap between DAAM and FasII localization, including the terminal area of the nerves innervating the body wall muscles (Fig. S1D-F). Consistent with this localization pattern and our published data (Matusek et al., 2008), 63% of the zygotically null mutant $DAAM^{Ex68}$ embryos displayed motoneuron growth and guidance defects, whereas the rest developed apparently normal terminals (Fig. S1G-I). Accumulation of DAAM protein was obvious in the third instar larval NMJs as well (Fig. 1A), whereas the staining was absent or much reduced in $DAAM^{Ex68}$ zygotically null mutant NMJs (Fig. S1J) (Matusek et al., 2006, 2008). Based on colocalization with the presynaptic HRP and the postsynaptic Discs large 1 (Dlg) markers, DAAM is present in both synaptic compartments (Fig. 1A), displaying a cortical accumulation. These protein localization data prompted us to probe the DAAM requirements during NMJ development directly.

DAAM is required for proper synaptic bouton formation

To begin our functional studies, we first performed a loss-of-function (LOF) analysis using the $DAAM^{Ex68}$ amorphic allele. As the *DAAM* locus resides on the X chromosome, we investigated hemizygous $DAAM^{Ex68}$ animals, most of which are early larval lethal although some reach the third larval instar stage with reduced body size and muscle area. NMJ morphology was visualized by immunostaining for routinely used presynaptic (HRP, Brp) and postsynaptic [Dlg, GluRIII (also known as GluRIIC)] markers. It has previously been shown that presynaptic bouton number scales with postsynaptic muscle area during NMJ growth (Aberle et al., 2002). Thus, to ensure an appropriate comparison, our NMJ analysis was carried out in L2 larvae in which the WT and $DAAM^{Ex68}$ mutant individuals did not show a significant difference in muscle size (Fig. 1J,K). We observed an ∼35% decrease in synaptic bouton number at muscle 4 in $DAAM^{Ex68}$ NMJs, as determined by HRP and Dlg staining (Fig. 1B, C,H). Because of its simple organization and easy accessibility, we concentrated on muscle 4 in our studies; nevertheless, a similar reduction in bouton number was observed at muscle 6/7 (Fig. 1E,F,I), indicating a general requirement for DAAM in NMJ development. In addition to the reduction in bouton number, NMJ length was also strongly reduced in the mutants (Fig. S2A,B), demonstrating its further requirement in axon terminal development.

The severe larval growth impairment in $DAAM^{Ex68}$ animals obviated the possibility for fine analysis of NMJs in these individuals. However, when we used a tracheal driver to express the full-length (FL) protein in a mutant background, generating a $DAAM^{Ex68}$*; btl-Gal4/UAS-FLDAAM* (hereafter $DAAM^{Ex68}$*; TR*) mutant combination, we were able to rescue the general growth deficit, including the reduced body and muscle size. In accordance with the fact that L3 larvae of these animals do not express the DAAM protein in neurons, we detected an ∼45% reduction in the number of synaptic boutons upon tracheal rescue of the *DAAM* null allele (Fig. 2A,B,G). Furthermore, there were atypical variations in bouton size, with interbouton stretches often appearing extended and frequently reaching the diameter of a bouton (a phenotype often termed ‘bouton fusion’) (Fig. 2B, quantified in Fig. 3D). To corroborate the requirement of DAAM for synaptic terminal development by an independent approach, we knocked down DAAM by RNAi in presynaptic and postsynaptic cells simultaneously with neuronal *elav-Gal4* in combination with the muscle-specific *Mef2-Gal4* line. We used two independent *DAAM*-specific RNAi constructs (with effective knockdown, Fig. S3A-E; see Materials and Methods), and both lines reduced bouton numbers (Fig. 2C,G; data not shown); similar to the effect observed in the $DAAM^{Ex68}$*; TR* mutant, bouton fusions were also evident. We next examined whether DAAM is required for NMJ development in the presynaptic neuronal cell or in the postsynaptic muscle cell. The RNAi experiment was repeated, but this time either presynaptically or postsynaptically. Presynaptic *DAAM* downregulation reduced bouton number (Fig. 2E-G), whereas muscle-specific knockdown had no discernible effects on bouton number (Fig. 2G) or NMJ morphology (Fig. 2D). As highly similar NMJ phenotypes were observed with both RNAi lines, these data revealed a presynaptic DAAM requirement for efficient bouton formation.

Development (2018) 145, dev158519. doi:10.1242/dev.158519

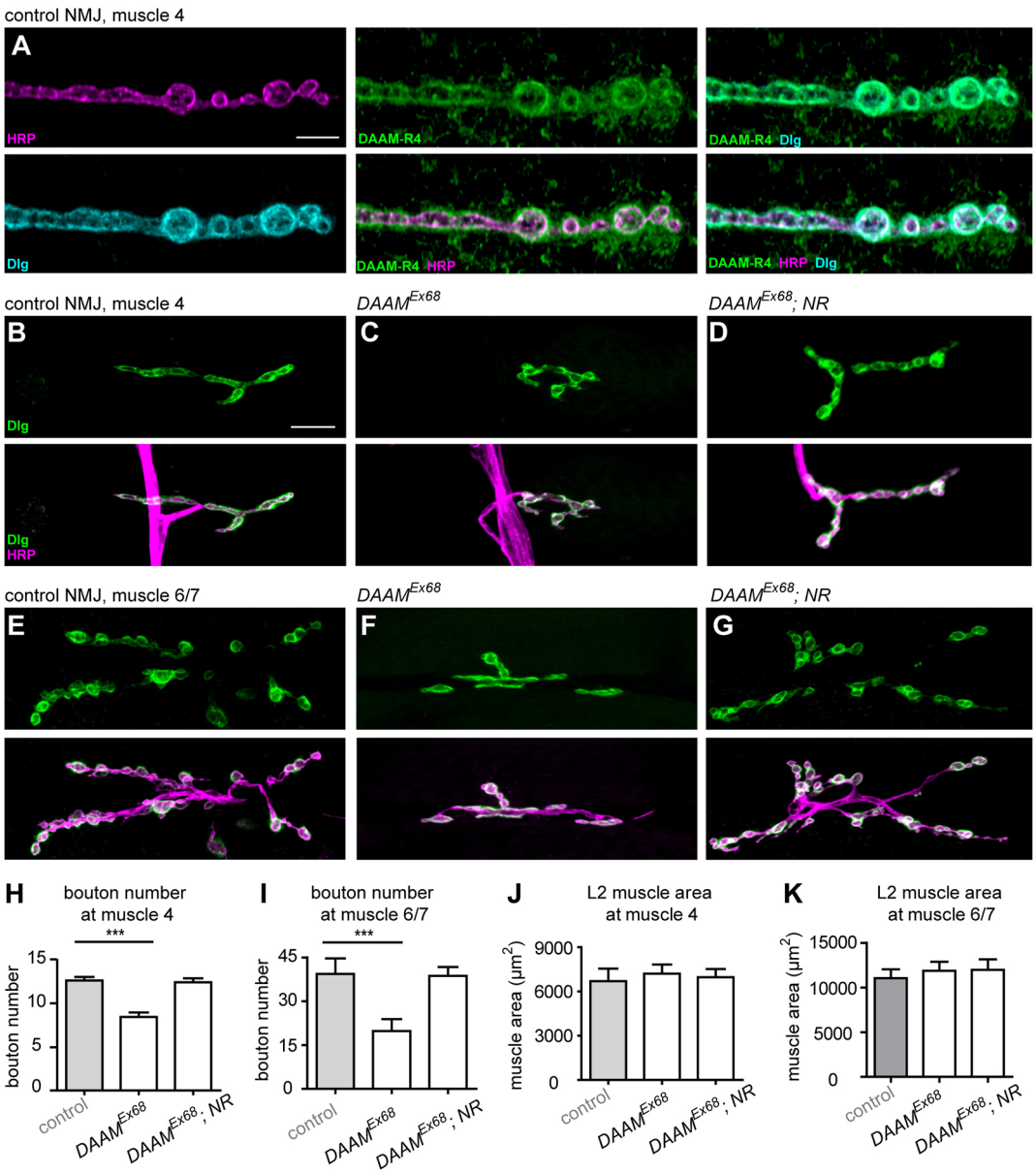

Fig. 1. DAAM is necessary for synaptic bouton formation. (A) Confocal immunofluorescence images of a third instar NMJ at muscle 4 from wild-type (WT) *Drosophila* larva stained with anti-DAAM-R4 (green), anti-Dlg (cyan) and anti-HRP (magenta) antibodies. (B-G) Second instar NMJs at muscle 4 (B-D) and muscle 6/7 (E-G) in w^{1118} control (B,E), $DAAM^{Ex68}$ (C,F) and $DAAM^{Ex68}$; *NR* ($DAAM^{Ex68}$;*UAS-FLDAAM*/+; *D42*/+) (D,G) animals visualized by anti-Dlg (green) and anti-HRP (magenta) staining. (H-K) Quantification of presynaptic bouton number (H,I) and muscle area (J,K) at muscle 4 (H,J) and muscle 6/7 (I,K) in larvae of the genotypes indicated ($n \geq 25$). Error bars indicate s.e.m. ***$P<0.001$. Scale bars: 5 µm in A; 10 µm in B-G.

To prove that these NMJ phenotypes were due to the lack of DAAM, rescue experiments were carried out in a $DAAM^{Ex68}$ background. When *UAS-FLDAAM* was expressed with the motoneuron-specific *D42-Gal4* driver, generating $DAAM^{Ex68}$; *D42-Gal4/UAS-FLDAAM* (hereafter $DAAM^{Ex68}$; *NR*), a nearly WT bouton number (Fig. 1D,G-I) and NMJ length (Fig. S2A,B) were restored. Together, these findings revealed a novel function of DAAM in CNS development linked to synaptic bouton formation. Furthermore, although the DAAM protein can be detected in both presynaptic and postsynaptic areas, these studies argue for a primarily presynaptic role.

DAAM is required for organization of presynaptic MTs

To better understand the presynaptic function of DAAM in synaptic terminal development, we analyzed the cytoskeletal elements in *DAAM* mutant NMJs. Based on our mass spectrometry analysis, Futsch, a widely used presynaptic MT marker, appeared to be a promising interaction partner of DAAM. Previous studies have established that Futsch promotes MT stabilization and new bouton formation (Hummel et al., 2000; Roos et al., 2000); therefore, we addressed whether lack of DAAM affected synaptic MT organization.

The presynaptic MT cytoskeleton in WT NMJs is organized into a prominent bundle of core filaments that becomes gradually thinner in the distal region of the presynaptic nerve terminal, as visualized by anti-Futsch immunostaining (Fig. 3A-Ab). Within $DAAM^{Ex68}$; *TR* mutant NMJs, however, the core MT bundle appeared fragmented and the MTs were often absent from the terminal boutons (Fig. 3B-Bb,E). Similar to $DAAM^{Ex68}$ mutant NMJs, the MT cytoskeleton was severely disorganized in the central area and

Development (2018) 145, dev158519. doi:10.1242/dev.158519

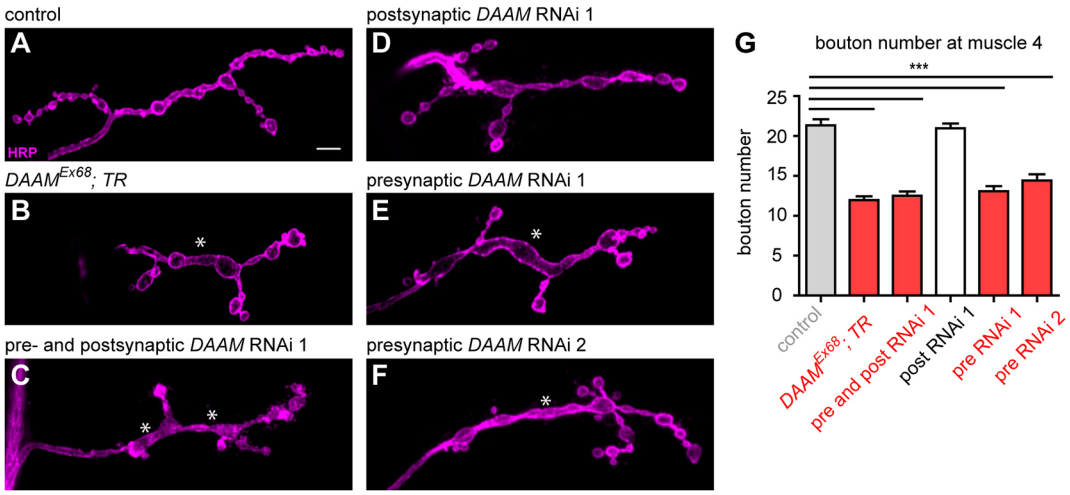

Fig. 2. A presynaptic requirement for DAAM in bouton formation. (A-F) NMJ terminals of muscle 4 stained with anti-HRP in third instar larvae. The NMJ terminals of control (*elav-Gal4*/+) (A) and postsynaptic *DAAM* RNAi 1 (*Mef2-Gal4*/+; *UAS-DAAM-RNAi 1*/+) (D) show normal interbouton organization, whereas in $DAAM^{Ex68}$; *TR* ($DAAM^{Ex68}$; *btl-Gal4, UAS-FLDAAM*/+) (B) or upon presynaptic and postsynaptic (*elav-Gal4*/+; *Mef2-Gal4*/*DAAM-RNAi 1*) (C) or presynaptic silencing of *DAAM* (*elav-Gal4*/+; *DAAM-RNAi 1*/+ and *elav-Gal4*/+; *DAAM-RNAi 2*/+) (E,F), a reduced bouton number and bouton fusion phenotype (asterisks) is evident. (G) Quantification of bouton numbers in the different *DAAM* mutants ($n \geq 25$). Error bars indicate s.e.m. ***$P<0.001$. Scale bar: 5 µm.

often retracted from terminal boutons in the nerve terminals upon presynaptic knockdown of DAAM (Fig. 3C-Cb,E). In addition to visualizing Futsch, we further confirmed the effect of DAAM by staining MTs directly with anti-Tubulin. Although MT organization in the terminal boutons was less evident with this marker, we detected frequent unbundling and fragmentation of the core MT

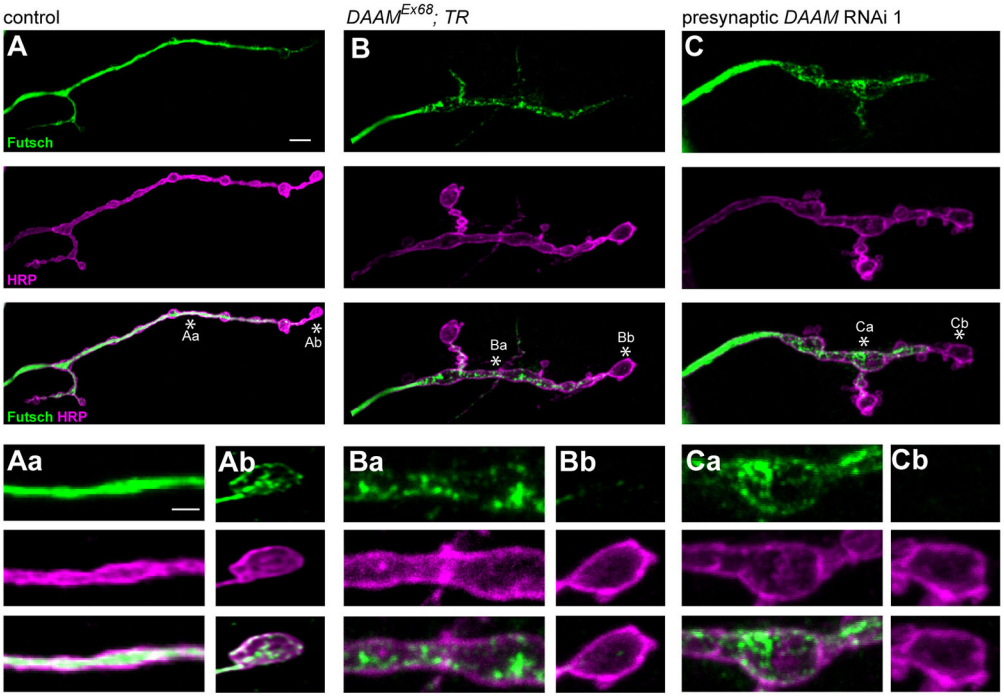

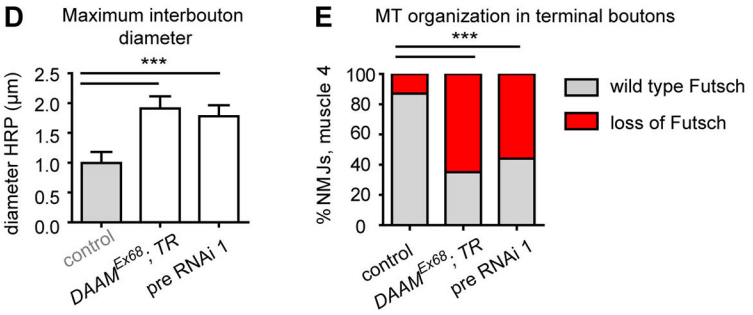

Fig. 3. Core MT organization is perturbed in *DAAM* mutant NMJs. (A-C) MT organization in control (*elav-Gal4*/+), $DAAM^{Ex68}$; *TR* ($DAAM^{Ex68}$; *btl-Gal4, UAS-FLDAAM*/+) and presynaptically silenced (*elav-Gal4*/+; *DAAM-RNAi 1*/+) NMJs at muscle 4 as judged by anti-Futsch (green) and anti-HRP (magenta) staining. Asterisks indicate central (a) and terminal (b) regions of control and *DAAM* mutant NMJs, as shown at high magnification beneath. MTs display a fragmented organization in *DAAM* mutant NMJs in the central region (Ba,Ca) and are often absent from the terminal region (Bb,Cb) as compared with *elav-Gal4*/+ controls (Aa,Ab). (D) Quantification of the diameter of the interbouton region in the central NMJ area ($n \geq 15$). (E) MT organization in terminal boutons ($n \geq 45$). Error bars indicate s.e.m. ***$P<0.001$. Scale bars: 5 µm in A-C; 2 µm in Aa-Cb.

Development (2018) 145, dev158519. doi:10.1242/dev.158519

filaments (Fig. S4A-Bb), virtually identical to that observed with anti-Futsch (22C10).

Previous studies have demonstrated that disruption of the MT cytoskeleton sometimes results in synaptic terminal disassembly or, ultimately, retraction of the presynaptic terminal (Koch et al., 2008; Pielage et al., 2008). To test this possibility, we visualized *DAAM*^{Ex68} mutant NMJs by immunostaining for the presynaptic AZ marker Brp and the postsynaptic protein GluRIII, which are juxtaposed in WT NMJs (Fig. S4C). We did not observe any alterations in the adjacent positioning of these markers in the mutant (Fig. S4D), indicating that loss of DAAM does not lead to presynaptic retraction. These data suggest that DAAM facilitates presynaptic MT stability and bouton/terminal outgrowth but it is dispensable for structural synapse terminal maintenance.

Although formins are best known for their ability to nucleate nascent actin filaments and promote their elongation, a growing body of evidence supports the fact that they are also involved in MT regulation (Bartolini and Gundersen, 2010; Chesarone et al., 2010); in particular, they have been implicated in MT stabilization in various cellular model systems (Bartolini et al., 2008; Cheng et al., 2011; Lewkowicz et al., 2008; Szikora et al., 2017; Wen et al., 2004). Therefore, we sought to identity which DAAM activities are important for NMJ development. We performed a series of rescue experiments with mutant versions of the full-length protein (FLDAAM), in which we impaired actin interaction alone or actin and MT interactions together. We used FLDAAM-I732A for the former (Gombos et al., 2015; Vig et al., 2017), mutating a conserved isoleucine residue within the FH2 domain crucial for actin interaction, while for the latter we created an FLDAAM-R876A-K881A double mutant, which is equivalent to the K989/994A mutation of mouse Dia1 that was shown to compromise both actin and MT regulation (Daou et al., 2014). Comparably to WT *UAS-FLDAAM*, when driven with *D42-Gal4* the *UAS-FLDAAM*^{I732A} mutant transgene could almost completely rescue the bouton number phenotype of *DAAM*^{Ex68} (Fig. 4A-D,F). By contrast, the *UAS-FLDAAM*$^{K876/881A}$ transgene failed to rescue the bouton number (Fig. 4E,F) and NMJ morphology (Fig. 4E) phenotypes of *DAAM*^{Ex68}. Given that *DAAM*^{Ex68} NMJs do not appear to exhibit overt alterations in actin organization (Fig. S5), we presume that the primary function of DAAM during NMJ development is related to its MT organizing role, whereas its F-actin assembly activity appears dispensable for synaptic bouton formation. Consistent with this scenario, we have recently revealed that DAAM has MT stabilization activity and binds to the plus end of MTs in primary neurons (Szikora et al., 2017).

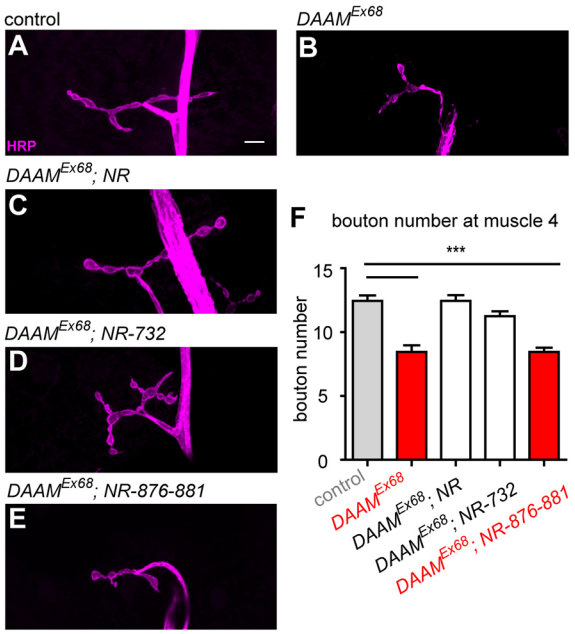

Fig. 4. The actin assembly activity of DAAM is dispensable for presynaptic bouton formation. (A-F) Presynaptic rescue analysis of *DAAM*^{Ex68} null mutant NMJs at muscle 4 in second instar larvae using *D42-Gal4* combined with WT and mutant *FLDAAM* transgenes. Anti-HRP was used as a presynaptic membrane marker. *w*^{1118} was used as WT control (A). The NMJ phenotype of *DAAM*^{Ex68} (B) can be rescued by WT *UAS-FLDAAM* (C), as well as with *UAS-FLDAAM*^{732}, a point mutant version that impairs actin binding (D). However, the *UAS-FLDAAM*$^{876-881}$ mutant version (impairing both actin and MT interactions) could not restore WT bouton numbers and NMJ morphology (E). (F) Quantification of the results of the rescue experiments shown in A-E in terms of synaptic bouton numbers ($n \geq 25$). Error bars indicate s.e.m. ***P<0.001. Scale bar: 5 µm in A-E.

The activated form of DAAM provokes excessive synaptic bouton formation

Based on LOF analysis, DAAM plays a role in NMJ development by promoting bouton formation. To strengthen this finding further, we tested whether an increased activity of DAAM would affect synapse formation. Formins are large, multidomain proteins, many of which are regulated by an intramolecular interaction between N- and C-terminal autoinhibitory domains, sterically blocking the activities of the FH2 domain (Wallar and Alberts, 2003). Removal of either of the autoinhibitory domains results in a constitutively active protein. In agreement with this, we demonstrated previously that C-DAAM, which lacks the N-terminal autoinhibitory domain, behaves as an activated DAAM form in the CNS (Gombos et al., 2015; Matusek et al., 2008). We show here that whereas pan-neural overexpression of FL-DAAM has no effect on NMJ morphology and MT organization in the terminal boutons (Fig. 5A-Bb), expression of C-DAAM increases synaptic bouton number in NMJs of third instar larvae (Fig. 5C,D). In addition, C-DAAM induces a greater variation in bouton size than is seen in WT, i.e. some boutons are large whereas others remain small and are partly decorated by so-called satellite boutons (Fig. 5C,Cb). It is also noteworthy that the interbouton area is often much wider than in WT (Fig. 5Aa,Ca). This phenotypic component, however, is similar to the LOF effect; in line with this, the core MT cytoskeleton is disrupted in the presence of activated DAAM (Fig. 5Aa,Ca). Thus, the effect of C-DAAM resembles a mixture of LOF and gain-of-function (GOF) phenotypes. Because formins function as obligate dimers, it is possible that C-DAAM interferes with the WT protein through dimerization, resulting in a dominant-negative LOF effect. Remarkably, however, C-DAAM clearly possesses a GOF effect with regard to bouton number, suggesting that this protein plays an instructive role in bouton formation.

DAAM interacts genetically with *wg* and *Ank2*

Prior studies have established that proper regulation of MT organization is crucial for synaptic bouton formation. Consistent with this, and similar to the effects of *DAAM* loss, mutations that disrupt MT organization also affect bouton number (Goellner and Aberle, 2012). Although none of the other known mutations altering synapse morphology exhibits an identical phenotype to that of *DAAM* mutation, strong parallels are evident, prompting an attempt to identify the signaling systems that regulate DAAM. We tested double mutant combinations of the major genes linked to synaptic MT regulation. First, the candidate genes were analyzed in a

Development (2018) 145, dev158519. doi:10.1242/dev.158519

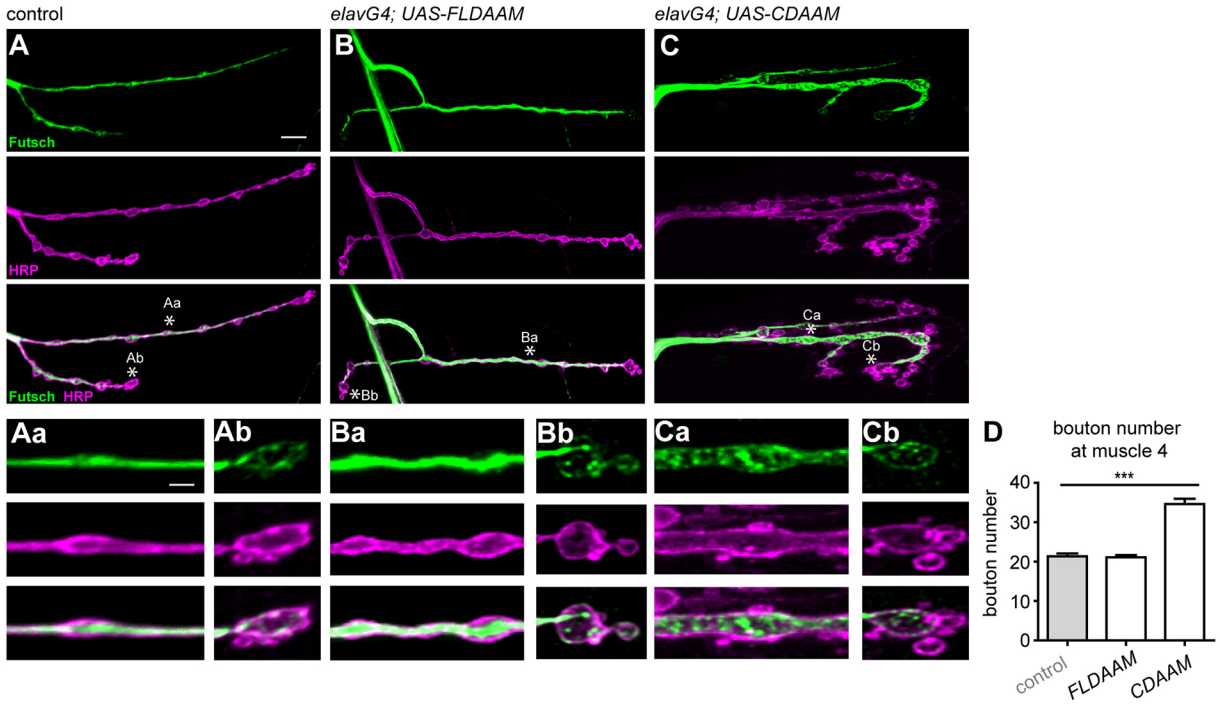

Fig. 5. Presynaptic overexpression of constitutively active CDAAM promotes new bouton formation. (A-C) Analysis of NMJ morphology in control (*elav-Gal4*) (A), *elav-Gal4/+; UAS-FLDAAM/+* (B) and *elav-Gal4/+; UAS-CDAAM/+* (C) larvae stained with anti-HRP and anti-Futsch. Asterisks indicate central (a) and terminal (b) regions of control and *DAAM* mutant NMJs, as shown at high magnification beneath. (D) Quantification of bouton numbers in control, *elav-Gal4; UAS-FLDAAM* and *elav-Gal4; UAS-CDAAM* animals in NMJs at muscle 4 in L3 larvae ($n \geq 25$). Error bars indicate s.e.m. ***$P<0.001$. Scale bars: 5 µm in A-C; 2 µm in Aa-Cb.

dominant genetic interaction assay in which $DAAM^{Ex68}$*; TR* was combined with heterozygous null mutations of *tkv*, *wg*, *Lar*, *dia* and *Ank2*. For initial assessment of the interactions, we quantified bouton number. The presence of a *tkv*, *Lar* or *dia* mutation did not change the reduced bouton number typical for loss of *DAAM* (Fig. 6A-D,I); however, the *wg* and *Ank2* mutations significantly reduced the bouton number (by ∼30% for *wg* and by ∼35% for *Ank2*) (Fig. 6F,H,I). Consistent with published data (McCabe et al., 2004; Pawson et al., 2008; Stephan et al., 2015), mutations of *wg* and *Ank2* alone in heterozygous conditions do not influence bouton number (Fig. 6E,G,J). Interestingly, DAAM has previously been linked to Wnt/Frizzled signaling in other cellular contexts (Gombos et al., 2015; Habas et al., 2001; Lee and Deneen, 2012). Moreover, previous studies have revealed that presynaptic Wg/Fz2 signaling (Miech et al., 2008) regulates the synaptic MT cytoskeleton in conjunction with Ank2 (Luchtenborg et al., 2014). Thus, these data support the notion that DAAM acts in concert with Wg and Ank2 during synapse development. Accordingly, among our candidate genes, it is the presynaptic impairment of the Wg pathway and of Ank2 function that most closely phenocopies *DAAM* mutants as manifest, in addition to the similar effect on bouton number, in bouton fusions/interbouton region dilations and MT unbundling (Luchtenborg et al., 2014; Packard et al., 2002; Stephan et al., 2015). Furthermore, our results suggest that Dia and DAAM might function independently during NMJ development. In agreement with this notion, unlike *dia*, *DAAM* does not exhibit an interaction with *trio* in a transheterozygous mutant combination (Fig. S6). Taking these studies together with the lack of interaction between *dia* and *DAAM* in double heterozygotes (Fig. S6), it appears likely that DAAM is controlled independently of the Lar/Trio/Dia module.

Previous work has placed Ank2 downstream of Wg signaling in synapses (Luchtenborg et al., 2014). We attempted to define the place of DAAM in this hierarchy by epistasis analysis in double hemizygous or homozygous mutants. As a preliminary experiment, we examined the phenotype of two *Ank2* alleles as control lines: $Ank2^{null}$, which affects both MT and synapse stability; and $Ank2\text{-}XL^{\Delta}$, an isoform-specific allele that selectively influences MT organization (Stephan et al., 2015). In accordance with previous results, these mutants exhibited reduced bouton numbers in parallel with bouton fusions and pronounced MT accumulations in the whole nerve terminal (Fig. 7A,A′, Fig. S7A,A′). By contrast, the strong MT aggregations were completely absent from *DAAM; Ank2* double mutants; instead, MTs organized into a central MT bundle that was nonetheless much thinner than in WT (Fig. 7B,B′, Fig. S7B,B′). Additionally, there was a drastic reduction in bouton numbers in $DAAM^{Ex68}$*; Ank2*^{null} NMJs, whereas the bouton number in $DAAM^{Ex68}$*; Ank2-*XL^{Δ} was only reduced to an extent comparable to that of $DAAM^{Ex68}$ (Fig. 7B, B′, Fig. S7B,B′). Interestingly, although both *Ank2* and *DAAM* single mutants displayed an enlarged interbouton region/bouton fusion phenotype (the diameter of the interbouton area is quantified in Fig. 7E), the typical ‘beads on a string’ bouton arrangement in *DAAM; Ank2* double mutants was restored, and small boutons, separated by thin interbouton areas, were clearly present (Fig. 7B,B′, Fig. S7B,B′). These results suggest a number of conclusions. Foremost, regarding the formation of aberrant MT aggregations and bouton number, *DAAM* is epistatic to *Ank2-XL*, which implies a downstream regulatory position. However, careful comparison of the MT phenotypes indicates that although *DAAM* can suppress the MT accumulations caused by the loss of *Ank2-XL*, the effect of *DAAM* on MT organization is dependent on Ank2-XL. If Ank2-XL is present, then the absence of *DAAM* induces MT fragmentation. By contrast, with concomitant loss of *Ank2-XL* and *DAAM*, the MT bundles are thinner but nonetheless nearly entirely continuous as compared with WT. Thus, MT organization in the double mutant is not identical to

Development (2018) 145, dev158519. doi:10.1242/dev.158519

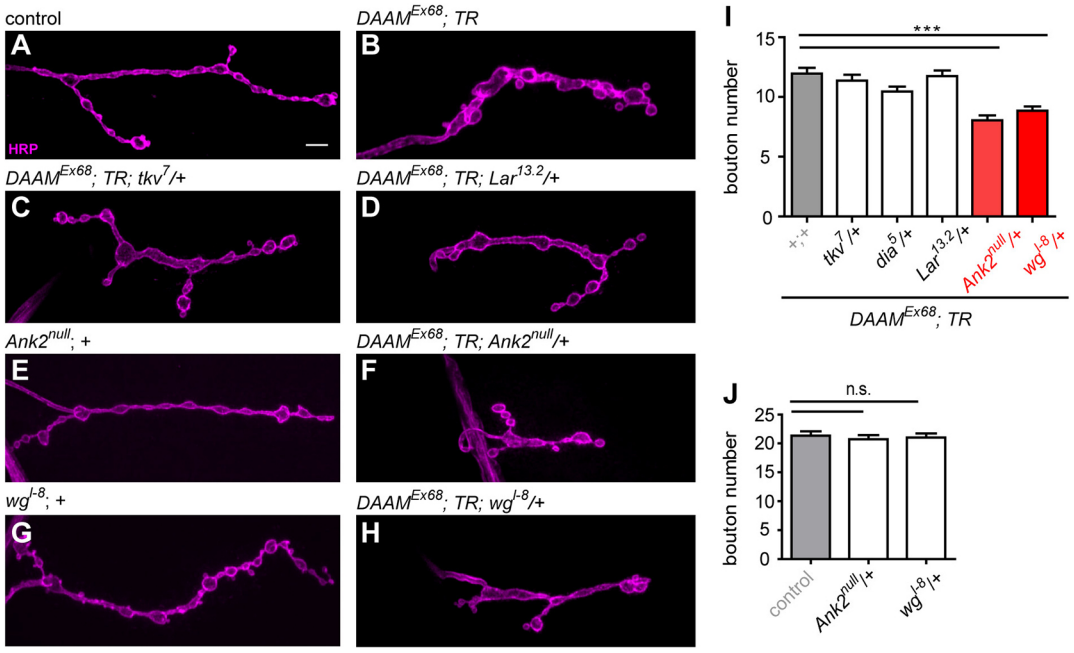

Fig. 6. *wg* and *Ank2* exhibit a dominant genetic interaction with *DAAM*. NMJs of control (w^{1118}) (A) and mutant L3 larvae of the genotypes indicated (B-H) stained with anti-HRP. (I,J) Quantification of bouton numbers in larvae in A-H. Note that when combined with $DAAM^{Ex68}$; *TR* (B) the heterozygous tkv^7, $Lar^{13.2}$ or dia^5 null mutations do not alter the reduced bouton number of $DAAM^{Ex68}$; *TR* (B-D,I). Conversely, one copy of wg^{l-8} and $Ank2^{null}$ could enhance (F,H,I) the bouton number defects of $DAAM^{Ex68}$; *TR* (B,I), indicating a dominant genetic interaction between these genes. As a control, loss of one copy of *Ank2* (E) or *wg* (G) alone does not change the bouton number compared with WT (A,J). $n \geq 25$. Error bars indicate s.e.m. ***$P<0.001$; n.s., not significant. Scale bar: 5 µm in A-H.

that of any of the single mutants, which is presumably key to the observed differences in bouton-interbouton organization. Collectively, these data are consistent with models involving a more complex interaction between Ank2 and DAAM than as part of a simple linear pathway.

Besides Ank2, the MT-stabilizing Futsch protein has also been shown to be a downstream effector of Wg signaling, and it is thought to function together with Ank2 to organize a membrane-associated MT-coordinating center (Luchtenborg et al., 2014; Stephan et al., 2015). To probe the regulatory connection between Futsch and DAAM, we analyzed *futsch* single and *DAAM, futsch* double mutants. As *DAAM* and *futsch* are both located at the tip of the X chromosome, we employed the CRISPR/Cas9 system to induce a *futsch* null mutation in both WT and $DAAM^{Ex68}$ mutant backgrounds, instead of taking a cumbersome recombination approach. Consistent with published data (Roos et al., 2000), NMJs of the novel null allele ($futsch^{CR13}$) were negative for anti-Futsch (22C10) immunostaining (Fig. S7C-E), and exhibited slightly reduced bouton numbers in parallel with a slight increase in bouton size (Fig. 7C, Fig. S7D) and in diameter of the interbouton region (Fig. 7C′,E), although with normal MT organization (Fig. 7C′). By contrast, the $DAAM^{Ex68}$, $futsch^{CR13}$ double mutant NMJs strongly resembled those of $DAAM^{Ex68}$ single mutants, with significantly reduced bouton numbers, the presence of bouton fusions, and fragmented MT organization (Fig. 7D,D′). Hence, *DAAM* is clearly epistatic to *futsch*, and these results argue for DAAM acting either downstream of Futsch or in a parallel pathway.

Synaptic transmission and AZ morphology are affected in *DAAM* mutant synapses

While analyzing the synaptic distribution pattern of the DAAM protein, two polyclonal DAAM antisera (R1 and R4) were compared that we had raised against the C-terminal half of the protein and which specifically recognize the DAAM protein in neurons (Fig. S8) (Gombos et al., 2015; Matusek et al., 2008) and in other tissues, such as the trachea (Fig. S9). Interestingly, unlike the R4 serum used above (Fig. 1A), DAAM formed discrete dots at the presynaptic plasma membrane (which were missing from null mutants and upon RNAi knockdown) with the R1 serum (Fig. S10A-B′, Fig. S3F,G), which resembled presynaptic AZs. Surprisingly, co-staining with an antibody against Brp, a core component of the presynaptic AZ scaffold (Fouquet et al., 2009), showed nearly perfect overlap with DAAM (Fig. S10A,A′). To achieve ultrastructural resolution, two-color, super-resolution stimulated emission depletion (STED) microscopy with ∼50 nm lateral resolution was used, which easily retrieved the typical ring-like distribution of the C-terminal Brp epitope residing at the distal aspect of the AZ scaffold. The DAAM signal also formed similar rings, which followed the Brp C-terminal signal very closely (Fig. 8A). Distance calculation of both signals in planar view showed that they are only ∼20 nm apart, with the DAAM signal shifted slightly into the interior of the Brp ring. Thus, we can conclude that discrete DAAM clusters form at the distal part of the AZ scaffold. Although DAAM protein stability was unaffected in *brp* mutants that eliminate scaffold assembly (Fig. S11), the DAAM signal at the AZs vanished (Fig. S10C,C′), indicating that DAAM clustering depends on an intact AZ scaffold. The question then arises as to whether DAAM clusters, with their connections to the actin and MT network, would be important to maintain AZ scaffold structure or function.

We first analyzed whether the AZ scaffold would be structurally or functionally affected after elimination of presynaptic DAAM. Previous work exploiting the high resolving power of STED microscopy showed that Brp adopts an extended conformation,

Development (2018) 145, dev158519. doi:10.1242/dev.158519

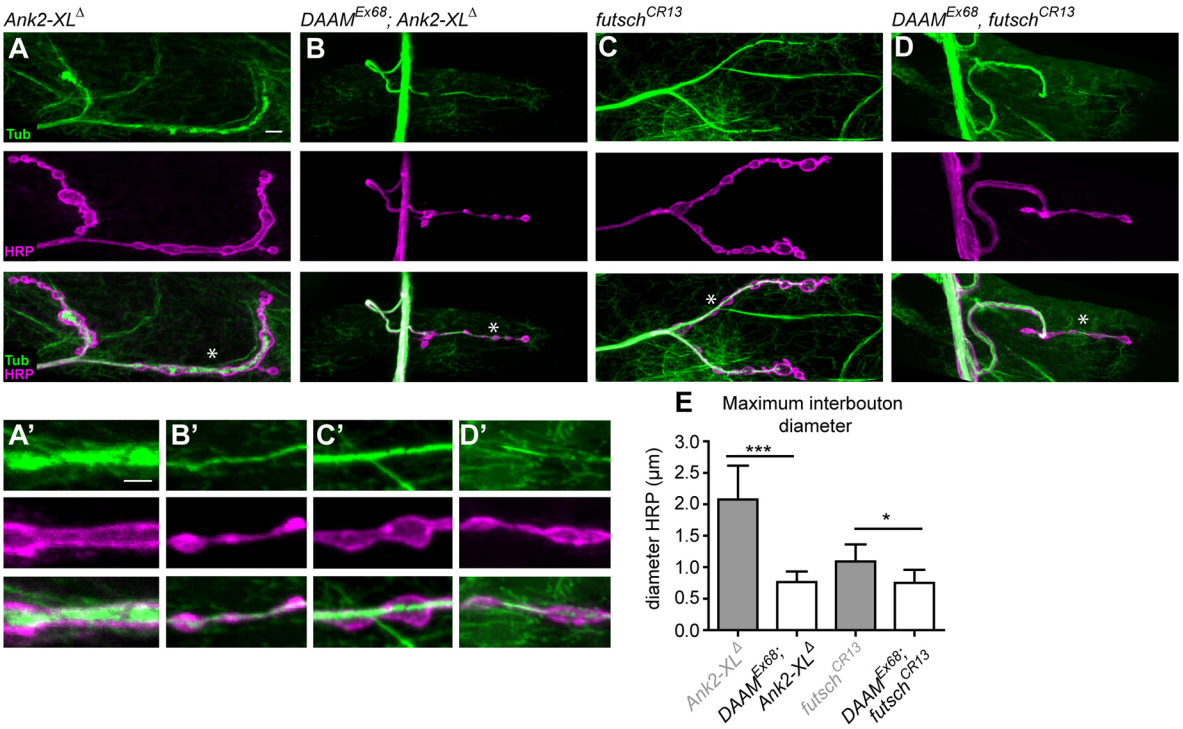

Fig. 7. Genetic epistasis analysis of *DAAM* with *Ank2* and *futsch*. (A-D) MT organization in NMJs of *Ank2-XL*$^{\Delta}$ (A), *DAAM*^{Ex68}*; Ank2-XL*$^{\Delta}$ (B), *futsch*^{CR13} (C) and *DAAM*^{Ex68}*, futsch*^{CR13} (D) mutant larvae visualized by anti-Tubulin and anti-HRP staining. (A′-D′) High magnification of central NMJ regions at muscle 4 as marked by asterisks in A-D. The bouton fusion and MT accumulation phenotypes of *Ank2-XL*$^{\Delta}$ (A,A′) were suppressed by *DAAM*^{Ex68} in the *DAAM*^{Ex68}*; Ank2-XL*$^{\Delta}$ double-mutant larvae (B,B′). NMJs of the *futsch*^{CR13} allele exhibit slightly reduced bouton numbers (C,C′), whereas the NMJ phenotype of the *DAAM*^{Ex68}*, futsch*^{CR13} double mutants (D,D′) is very similar to that of *DAAM*^{Ex68} single mutants with regards to both bouton number reduction and bouton fusion. (E) Quantification of diameter of the interbouton region in the central NMJ area as judged by anti-HRP staining ($n \geq 45$). Error bars indicate s.e.m. *$P<0.05$, ***$P<0.001$. Scale bars: 5 µm in A-D; 2 µm in A′-D′.

with its N-terminus facing towards the AZ plasma membrane and the C-terminus into the bouton interior. We used two-channel STED to visualize AZ scaffold organization and size by co-staining for Brp C-terminal and N-terminal epitopes. In the *DAAM*^{Ex68} mutant, the Brp scaffolds appeared essentially similar to control scaffolds (Fig. 8B,C). Using electron microscopy, we characterized electron-dense T-bars representing the AZ scaffold. Quantification of Brp ring diameter (Fig. 8K) and T-bar roof size revealed only a slight, non-significant upward trend in the *DAAM* mutant (Fig. 8D,E,L). However, SV densities close to the AZ membrane (within 200 nm of the AZ center) were slightly but significantly reduced in *DAAM* mutants (Fig. 8M).

Finally, we examined whether DAAM LOF could influence the efficiency of synaptic transmission due to its prominent localization close to the sites of neurotransmitter release. Two-electrode voltage clamp experiments (TEVC) were performed in *DAAM*^{EX68}*; TR* mutants. Although spontaneous release was not altered (Fig. 8G,I,J), we observed a moderate but significant reduction (by 19%) in evoked excitatory NMJ currents (Fig. 8F,H). In summary, DAAM is robustly associated with the AZ scaffold, and its absence impairs SV release. Its exact role in SV release should be an interesting subject for further studies.

DISCUSSION

Here, we identified DAAM, a formin type of cytoskeleton regulatory protein, as a novel factor required for NMJ development in *Drosophila*. Unexpectedly, the F-actin assembly activity of DAAM is not essential for synaptic terminal growth; instead, DAAM is necessary for MT organization, and deficits in proper MT organization are likely to be responsible for the deficits in bouton growth that we observed. In accordance with this, genetic interaction analyses suggest that DAAM acts together with the Wg/Ank2/Futsch module, which is known to control presynaptic MT regulation and bouton formation. In addition, we provide novel evidence that, besides a role in terminal arbor development, DAAM is tightly associated with the synaptic AZ scaffold. It is recruited to synaptic AZs in a Brp-dependent manner, and our electrophysiological data are consistent with a modulatory function in synaptic activity. Thus, this formin appears to be an interesting player in synaptic terminal development that not only promotes presynaptic bouton growth but also contributes to synapse function at the vesicle release site.

DAAM and Dia: two formins with different presynaptic roles?

An important prior study established that Dia, another member of the formin family, is pivotal for synaptic growth (Pawson et al., 2008). Although Dia is present both presynaptically and postsynaptically, published data support that it has a presynaptic function in bouton formation. The zygotic absence of Dia leads to a decrease in bouton number in parallel with an increase in bouton area. Defects were reported in both the actin and MT cytoskeleton, and genetic studies placed *dia* downstream of *Lar* and *trio* in the control of NMJ growth. By comparison, DAAM also functions presynaptically and its loss reduces bouton number. However, a bouton fusion phenotype is also evident in *DAAM* mutant NMJs that is not observed in *dia* mutants. Moreover, unlike *dia*, defects in actin organization are not obvious in *DAAM* mutants and, consistently, the actin polymerization-incompetent form of DAAM is still able to rescue the synaptic terminal growth defects. By contrast, a role in MT organization is apparent from both formin mutants, albeit with

Development (2018) 145, dev158519. doi:10.1242/dev.158519

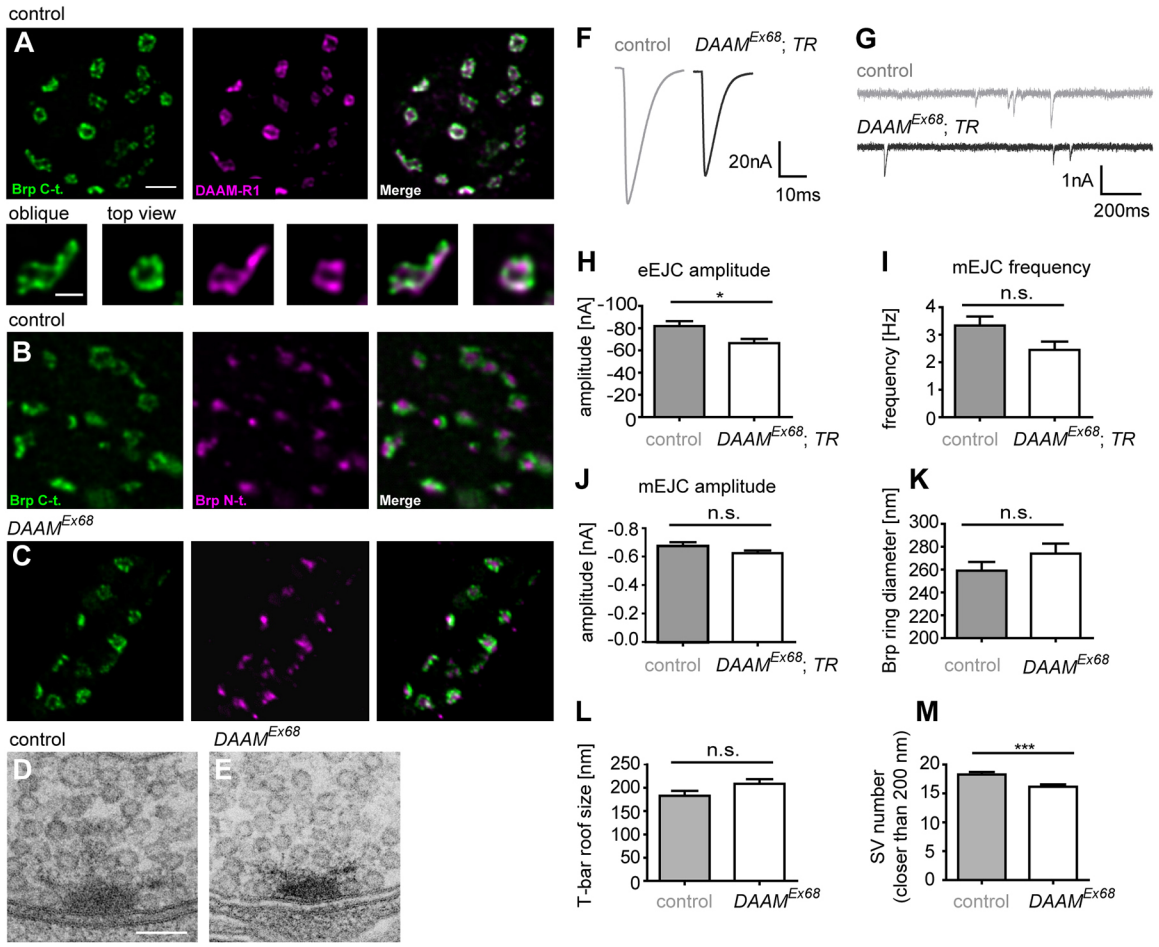

Fig. 8. Lack of *DAAM* influences SV release and AZ morphology. (A) STED microscopy revealed that DAAM is tightly associated with the distal part of the AZ scaffold in NMJs, as stained with anti-DAAM-R1 and Brp C-terminal (nc82) antibodies. (B,C,K) Comparison of AZ morphology (visualized by anti-Brp N-terminal and C-terminal antibodies) in control (w^{1118}) (B) and $DAAM^{Ex68}$ mutant (C) synapses does not show significant differences, as quantified in terms of Brp ring diameter (K). (D,E) Ultrastructural analysis of the AZ (T-bar) in control (D) and $DAAM^{Ex68}$ mutant (E) animals. (F-J) TEVC analysis of control and $DAAM^{Ex68}$*; TR* mutant synapses at muscle 6/7. Evoked excitatory potential was significantly reduced in *DAAM* mutant NMJs compared with WT (F,H); however, the lack of *DAAM* did not alter spontaneous release (G,I,J). (L) Quantification of T-bar roof size in control and $DAAM^{Ex68}$ mutants. (M) Quantification of SV number close to the AZ (within 200 nm of the AZ center) in control and $DAAM^{Ex68}$ larvae. Error bars indicate s.e.m. *P<0.05, ***P<0.001. (H-J) $n\geq10$, (K-M) $n\geq70$. Scale bars: 750 nm in A (top),B,C; 250 nm in A, oblique and top views; 100 nm in D,E.

clearly different effects, as *DAAM* mutation causes an MT fragmentation phenotype (this study), whereas *dia* mutation impairs the behavior of a dynamic pioneer MT population (Pawson et al., 2008) without gross effects on MT organization. Lastly, it is notable that the phenotypic similarities and genetic interaction studies both connect DAAM to the Wg/Ank2 cortical cytoskeletal system. Therefore, it appears that, despite their very similar domain structure and partially related phenotypic effects, these two formins are likely to play distinct roles during NMJ development. Consistently, they seem to be controlled by different signals, and whereas Dia is involved in the modulation of MT dynamics (and, possibly, actin regulation), DAAM is required for central MT bundle stabilization.

The interplay of Wg, Ank2, Futsch and DAAM in presynaptic MT regulation

Proper coordination of presynaptic MT dynamics is thought to be key to synaptic differentiation, including bouton formation. MTs are regulated by a number of signaling pathways, including the Wg/Wnt pathway (Budnik and Salinas, 2011), as well as by MT-associated proteins such as Futsch/MAP1B. Current evidence suggest that a divergent branch of the canonical Wg pathway (comprising Wg, Fz2, Arr, Gαo, Dsh and Sgg) is at work to locally regulate MT stability on the presynaptic side of *Drosophila* NMJs. This is achieved, at least in part, by inhibition of the Ser/Thr kinase Sgg, which has been proposed to regulate MT stability by phosphorylation of Futsch (Gögel et al., 2006). Interestingly, the founding member of the DAAM formin subfamily, Daam1, has been characterized as a Dsh-associated Wnt signaling component (Habas et al., 2001). Although initial work placed Daam1 in the non-canonical Wnt/PCP (planar cell polarity) pathway, subsequent studies found a link to the canonical branch as well (Lee and Deneen, 2012), suggesting that DAAM proteins might be more versatile components of the pathway. In support of the possibility that DAAM is part of the MT-regulating branch of the Wg pathway, we revealed that *DAAM* and *wg* exhibit a dominant genetic interaction. Moreover, the NMJ phenotype of *DAAM* is most similar to that of mutations affecting the Wg pathway, both with regard to bouton fusions and the fragmented/punctate MT organization. Along with Wg, Ank2 has also been shown to play an essential role in the regulation of MT dynamics and organization. A recent study demonstrated a differential requirement for two giant Ank2

Development (2018) 145, dev158519. doi:10.1242/dev.158519

isoforms in the process: Ank2-L controls MT and synapse stability upstream of Ank2-XL, which appears to control MT organization synergistically with Futsch (Stephan et al., 2015). However, in contrast to Wg pathway mutants, even if bouton fusions are evident, the loss of *Ank2-XL* results in the formation of prominent MT aggregates rather than MT fragmentation. Based on genetic, biochemical and protein localization data, Ank2 and Futsch were placed downstream of Wg/Fz2/Sgg, whereas the double LOF mutant analysis of *Ank2* and *futsch* suggested that Ank2-XL controls MT organization upstream and synergistically with Futsch. Where is DAAM in this hierarchy? Based on genetic epistasis analysis, LOF mutation of *DAAM* clearly suppresses the MT aggregation phenotype of *Ank2-XL*, but only a weak central MT bundle forms and boutons no longer exhibit a fused appearance. Thus, similar to Futsch, DAAM is required for MT aggregation in the absence of Ank2-XL, which would place it downstream of Ankyrin as an MT-stabilizing factor. However, the two other major phenotypic effects (not detected in either of the single mutants) presumably indicate a more complex regulatory connection. By contrast, the NMJ phenotype of the *DAAM, futsch* double mutant is nearly identical to that of the *DAAM* single mutant. Collectively, we interpret these data as indications that Wg/Fz2 signaling is likely to govern MT organization through several parallel effectors, including Ank2, Futsch and DAAM, and that these proteins might operate in a complex, regulating different aspects of MT dynamics in a concerted manner, rather than through a simple linear regulatory cascade.

Cytoskeleton organization at AZs: the potential role of DAAM

In addition to detecting an effect on MT stabilization and synaptic terminal morphology, we observed a reduction in evoked amplitudes that is associated with a reduced abundance of SVs in the vicinity of AZs, suggesting that *DAAM* mutation reduces the number of SVs accessible for evoked release. Although this is a relatively modest effect, a pool of DAAM protein was found to be specifically positioned at AZs. The application of STED microscopy allowed us to determine that this formin protein is enriched in a ring-like pattern in the immediate vicinity of the C-terminus of Brp, a major AZ scaffold protein. Furthermore, we have demonstrated a requirement of Brp for DAAM localization, but not vice versa. Together, these observations highlight a potential novel DAAM function in connecting MT organization with AZs. Intriguingly, Futsch was recently shown to localize close to the AZ scaffold, and to link AZs to the MT cytoskeleton (Lepicard et al., 2014). Similar to *DAAM* LOF, *futsch* LOF also resulted in deficits in SV release. It is tempting to speculate that Futsch and DAAM cooperate as a module connecting the AZ scaffold with MTs projecting towards AZs, and thus provide efficient trafficking of SVs. Another interesting line of recent research revealed a role for the divergent canonical Wg pathway in remodeling the presynaptic AZs in *Drosophila* photoreceptor cells (Sugie et al., 2015). Most notably, this module was shown to form a major effector pathway downstream of light stimulation in regulating the molecular composition of synapses *in vivo*. Remarkably, Futsch-dependent MT reorganization is also required for AZ remodeling in this system. Thus, it remains an interesting question for future research whether the local DAAM spots of the AZ scaffold cooperate with Futsch or contribute to AZ function by other means.

In addition to the potential role of MTs, dynamic assembly of F-actin has a well-established role in SV release, and actin is a known component of the AZ cytomatrix (Hirokawa et al., 1989; Li et al., 2010; Morales et al., 2000; Phillips et al., 2001). Although the regulation of actin assembly at AZs is largely uncharacterized, the AZ cytomatrix protein Piccolo has recently been implicated as an important regulator of presynaptic actin assembly in vertebrate neurons by providing a platform for various actin-binding proteins (Kim et al., 2003; Wagh et al., 2015; Waites et al., 2011; Wang et al., 1999), including Daam1, the rat ortholog of *Drosophila* DAAM. Based on neuronal culture experiments, it was proposed that activated Daam1 is recruited by Piccolo and that they direct activity-dependent F-actin assembly at the AZs (Wagh et al., 2015). Despite the fact that we observed no alterations in F-actin organization in *DAAM* mutant NMJs and that the actin assembly activity of DAAM is dispensable for NMJ growth, our present data do not exclude the possibility that DAAM plays an actin-modulating role at the AZs. In light of our recent findings in axonal growth cones (Szikora et al., 2017), an appealing alternative model is that DAAM plays a role in mediating actin-MT crosstalk at the neurotransmitter release sites. Although further experiments are clearly required to distinguish between these alternatives, we conclude that DAAM family formins are likely to be evolutionarily highly conserved factors that link the synaptic AZ scaffold to cytoskeletal remodeling.

MATERIALS AND METHODS

Drosophila stocks, genetics and molecular biology

Flies were raised at 25°C under standard conditions. The following mutant strains were used: #3605 w^{1118}, #39058 *P(TRiP.HMS01978)attP2* (designated as DAAM-RNAi 2), #27390 *Mef2-Gal4*, #8816 *D42-Gal4*, #458 $elav^{C155}$*-Gal4*, #3242 tkv^{7}, #8774 $Lar^{13.2}$, #5351 wg^{l-8}, #8805 $futsch^{N94}$ and #9138 dia^{5}, all provided by the Bloomington *Drosophila* Stock Center; $DAAM^{EX68}$ (Matusek et al., 2006), *btl-Gal4* (kind gift from C. Samakovlis, Stockholm University, Sweden), $futsch^{K68}$ (kind gift from M.-L. Parmentier, Institute for Functional Genomics, Montpellier, France), $brp^{\Delta 6.1}$ (Matkovic et al., 2013), brp^{69} (Kittel et al., 2006), $Ank2^{518}$ (used as a null allele) and $Ank2\text{-}XL^{A}$ (kind gift from J. Pielage, Technical University of Kaiserslautern, Germany).

The $UAS\text{-}CDAAM^{3xFlag}$ (random insertion) was created using pENTR3c-CDAAM (Matusek et al., 2008) to generate a pTWF-UAS-CDAAM destination construct, which was randomly integrated into the genome (a second chromosomal insertion was employed). The *P{UAS-FLDAAM}attPVIE-260B*, $P\{UAS\text{-}FLDAAM^{732}\}attPVIE\text{-}260B$ and $P\{UAS\text{-}FLDAAM^{876\text{-}881}\}attPVIE\text{-}260B$ lines were created using pENTR3c-FLDAAM (Matusek et al., 2008), pENTR3c-FLDAAM^{732} (primers listed in Table S1) and pENTR3c-FLDAAM$^{876\text{-}881}$ (primers listed in Table S1) entry clones, respectively, to generate the corresponding final clones in pTWattB (kind gift from L. Kovács, University of Cambridge, UK), which were subsequently integrated into the same genomic position (attP-VIE-260B) with phiC31. The *P{UAS-shRNA-DAAMFH2}attP2* (designated DAAM-RNAi 1) transgenic strain was generated through standard cloning methods and *in vitro* mutagenesis (primers listed in Table S1) in pValium20 vectors (DRSC/TRiP Functional Genomics Resources).

The $DAAM^{3xFlag}$ knock-in allele was produced by a gene conversation method described previously (Molnar et al., 2014). The $futsch^{CR13}$ single and $DAAM^{Ex68}$*,* $futsch^{CR13}$ double mutants were generated by the CRISPR/Cas9 technique (Gratz et al., 2013). Two 20 nt gRNAs were designed (primers listed in Table S1) with homology to the 5′ and 3′ ends of the first coding exon of *futsch* located 300 bp apart. After germ cell-specific simultaneous expression of Cas9 and the gRNAs in a WT and a *DAAM* mutant background, we collected *futsch* mutant candidates from the second generation, which were validated by PCR and sequencing. Based on the sequencing data, the expected ∼300 bp deletion was detected in the first coding exon of the mutant strains. Analysis of $futsch^{CR13}$ by anti-Futsch (22C10) immunostaining and western blot revealed that this allele behaves as a protein null allele (Fig. S7C-E).

Immunohistochemistry

For larval NMJ analysis, second and third instar larvae were dissected in PBS and fixed in 4% paraformaldehyde (PFA) for 20 min. For DAAM-R1,

Development (2018) 145, dev158519. doi:10.1242/dev.158519

acetylated-Tubulin, Futsch and GluRIII stainings, the dissected larval fillets were fixed in methanol for 5 min. The samples were then washed in PBS containing 0.1% Triton X-100 (PBST) three times for 20 min each and blocked in PBST with 0.2% BSA (PBS-BT) for 2 h. Primary and secondary antibodies were diluted in PBS-BT and incubated overnight at 4°C. The following primary antibodies were used: rabbit anti-HRP (Jackson) 1:200 and goat anti-HRP Alexa 647 (Jackson) 1:600 used as presynaptic membrane markers, mouse anti-Dlg (DSHB, 4F3) 1:100, mouse anti-Futsch (DSHB, 22C10) 1:200, rabbit anti-GluRIII (Marrus et al., 2004) 1:1000, rabbit anti-Futsch C terminus (kind gift from Christian Klämbt, University of Münster, Germany) 1:1000, mouse anti-Brp C-terminus (DSHB, nc82) 1:100, mouse anti-acetylated Tubulin (Sigma, 6-11B-1) 1:1000, rabbit anti-DAAM-R1 (Matusek et al., 2006) 1:1000, and rabbit anti-DAAM-R4 (Gombos et al., 2015) 1:500. Secondary antibodies coupled to Alexa 488, Alexa 546 and Alexa 647 were used (Thermo Fisher Scientific).

For embryonic NMJ analysis, embryos were fixed as previously described (Matusek et al., 2006). The following primary antibodies were used in immunostaining: rabbit anti-DAAM-R4 (Gombos et al., 2015) 1:200, mouse anti-BP102 (DSHB) 1:500, rat anti-DCAD2 (DSHB) 1:100, and mouse anti-FasII (DSHB, 1D4) 1:50. For HRP staining, we used the Vectastain ABC Kit (Vector Laboratories).

Mass spectrometry analysis

Protein mixtures isolated by immunopurification were separated using SDS-PAGE. WT and DAAM-Flag lanes were cut into 12 pieces each and subjected to in-gel digestion with trypsin (for the detailed protocol, see the supplementary Materials and Methods). The resulting peptide mixtures were analyzed by LC-MS/MS using a Waters nanoAcquity UPLC on-line coupled to an Orbitrap-Elite mass spectrometer (Thermo Fisher Scientific) operating in the positive ion mode. After trapping at 3% B (Waters Symmetry C18 180 µm×20 mm column, 5 µm particle size, 100 Å pore size, flow rate of 10 µl/min), peptides were separated with a linear gradient of 10-40% B in 90 min (using a 75 µm×104 mm column self-packed with MagicC18AQ, 3 µm particle size, 200 Å pore size, solvent A comprising 0.1% formic acid/water, solvent B comprising 0.1% formic acid/ACN, flow rate of 400 nl/min). Data acquisition was carried out in a data-dependent fashion; the ten most abundant multiply charged ions were selected from each MS survey scan (m/z, 380-1600) for MS/MS analyses with CID activation (normalized collision energy, 35). MS spectra were acquired in the Orbitrap, and CID spectra in the linear ion trap. Dynamic exclusion was enabled (exclusion time, 30 s).

Raw data were converted into peak lists using PAVA software (Guan et al., 2011) and searched with the ProteinProspector search engine (v.5.19.4, http://prospector.ucsf.edu), applying the following parameters: mass accuracy, 5 ppm for precursor ions and 0.6 Da for fragment ions (both specified as monoisotopic values); enzyme, trypsin with maximum of one missed cleavage site; fixed modifications: carbamidomethyl (Cys); variable modifications: Met oxidation, pyroGlu formation from N-terminal Gln residues and acetylation of protein N-terminus (maximum two variable modifications/peptide); instrument, ion trap. First, the Swiss-Prot database was searched, then the contaminants identified were appended to the *Drosophila melanogaster* entries of the UniProt database concatenated with a randomized sequence for each entry (downloaded 6 Sept 2016, 42,488 protein sequences). Acceptance criteria: score, 22 and 15; E-value, 0.01 and 0.05 for protein and peptide identifications, respectively.

Relative abundance of proteins was estimated by spectral counting; peptide counts of the proteins were normalized to the total number of peptides identified in each sample, then the normalized peptide counts were compared between the two samples. Normalized peptide count ratios were corrected using the median value of normalized peptide count ratios. A protein was considered overrepresented in any of the samples if the median corrected normalized peptide count ratio was at least twice that in the other sample.

Western blot

Adult heads were homogenized in RIPA buffer (0.1% SDS, 0.2% Na deoxycholate, 0.05% NP40, 150 mM NaCl, 50 mM Tris-HCl, pH 7.4). After centrifugation, SDS sample buffer was added to the lysates and the samples were separated on standard SDS-PAGE gels (6%). Proteins were then transferred onto PVDF membranes, which were stained with the following primary antibodies: rabbit anti-DAAM-R4 (Gombos et al., 2015; 1:500), mouse anti-Flag (Sigma, M2, 1:500), mouse anti-Futsch (DSHB, 22C10, 1:100) and rabbit α-glycogen phosphorylase (1:20,000; kindly provided by A. Udvardy, Biological Research Centre, Szeged, Hungary). After three washing steps, the membranes were incubated with HRP-conjugated anti-rabbit (Jackson, 1:10,000) and anti-mouse (DAKO, 1:5000) secondary antibodies. After secondary antibody staining, the PVDF membranes were visualized with chemiluminescent reagents (Immobilon Kit, Millipore).

Image analysis and quantification

Confocal images were acquired either on an Olympus FV-1000 laser scanning microscope or on a Zeiss LSM 880. Images were restored by Huygens deconvolution software (Scientific Volume Imaging). ImageJ (http://rsbweb.nih.gov/ij)/FIJI software was used to quantify the various parameters of NMJs.

Quantification of NMJ bouton number, length and muscle area

NMJs of muscles 4 and 6/7 from abdominal segments 2-5 (A2-5) were analyzed in all cases in at least ten individual larvae from each genotype. Either two or three NMJs were used per animal for quantification of bouton number, NMJ length and muscle area, and in this way we analyzed at least 25 individual NMJs for each genotype and parameter measured. One bouton was identified as a circular or oval structure of an axon terminal visualized by anti-HRP/Dlg staining. NMJ length was measured as the distance between the two farthest points of the NMJ determined with the help of anti-HRP staining. Overview images were taken from each NMJ, which were subsequently used for quantification of bouton number and NMJ length. Based on the overview images, muscle area of each NMJ was measured based on the Dlg signal with the polygon selection tool of the FIJI software.

Quantification of interbouton diameter

The interbouton region was identified as a bridge-like structure of the NMJ that connects two boutons, and which is completely filled with MTs in a WT NMJ but contains less compactly organized MT bundles in *DAAM* mutants. For quantification of the diameter of the interbouton areas, the middle third stretch of the NMJ at muscle 4 in segments A2-3 was used. Measurements were carried out on three neighboring interbouton regions in each sample; the maximum diameter of these defined interbouton areas was measured based on staining with anti-HRP. At least 15 samples (45 interbouton regions) were analyzed for each genotype examined.

Quantification of MT organization in terminal boutons

In most WT terminal boutons, MTs can clearly be detected, although MT organization usually lacks prominent bundles and appears rather dispersed as determined by anti-Futsch staining. Images of terminal boutons (e.g. Fig. 3) were acquired with identical confocal settings for each sample, using the complete dynamic range of the detectors to avoid clipping. Brightness and contrast of the images in Fig. 3Ab,Bb,Cb were linearly adjusted in FIJI to enhance the information that is already present in the original images (Fig. 3A-C) in the lower end of the 16-bit intensity range. By analyzing 25 terminal bouton images for each relevant genotype, we detected the presence of MTs in ∼86% of WT boutons and in ∼40% of *DAAM* mutant boutons.

STED microscopy

Preparation and staining were performed as previously described (Owald et al., 2010). All larvae were fixed for 5 min with ice-cold methanol. Primary antibodies were mouse monoclonal anti-Brp C-terminal (1:250, Nc82, DSHB), rabbit anti-Brp N-terminal (1:100) (Fouquet et al., 2009), and rabbit anti-DAAM-R1 (1:2000) (Matusek et al., 2006). Secondary antibodies were goat anti-mouse Atto647N (1:500, ATTO-TEC) and goat anti-rabbit Alexa 594 (1:500, Thermo Fisher Scientific). Larvae were mounted in ProLong Gold antifade mountant (Thermo Fisher Scientific).

Two-color STED images were taken with a TCS SP8 gSTED (Leica Microsystems) equipped with a tunable white light laser (470-670 nm), a depletion laser at 775 nm, and HC PL APO CS2 100× objective (oil immersion, NA 1.4). STED images were acquired with LAS X software

Development (2018) 145, dev158519. doi:10.1242/dev.158519

(Leica Microsystems) and batch deconvolved using Huygens Professional deconvolution software. The point spread function for deconvolution was generated with a 2D Lorentz function with its half-width and half-length fitted to the half-width and half-length of a sample image. Measurements of Brp ring diameters were performed on deconvolved images using ImageJ. The images were set to a threshold value in order to obtain a realistically shaped binary mask of the planar oriented Brp rings. Magic Wand tool was used to select the outline of each ring as a region of interest (ROI). A custom script was used to extrapolate the diameter of each ROI from its area using the formula of a perfect circle: $d=2\times\sqrt{(A/\pi)}$.

Electrophysiology

TEVC recordings were carried out essentially as previously reported (Qin et al., 2005). All experiments were performed on male third instar larvae raised at 25°C. Dissection and recording medium was extracellular hemolymph-like solution 3 (HL3) (70 mM NaCl, 5 mM KCl, 20 mM $MgCl_2$, 10 mM $NaHCO_3$, 5 mM trehalose, 115 mM sucrose, 5 mM HEPES, pH 7.2). Dissection was performed in ice-cold Ca^{2+}-free HL3 medium, whereas recordings were performed in 1.5 mM Ca^{2+} HL3 at room temperature. Evoked (eEJCs) and miniature (mEJCs) excitatory junction currents were recorded at muscle 6 of abdominal segment A2/A3 using intracellular electrodes with resistances of 15-20 MΩ (filled with 3 M KCl). Recordings were low-pass filtered at 1 kHz and sampled at 10 kHz. mEJCs were recorded at a voltage clamp of −80 mV; for eEJC measurements cells were voltage clamped at −60 mV and stimulated at 0.2 Hz. Only cells with an initial membrane potential (V_m) between −50 and −70 mV and input resistances of ≥4 MΩ were used for further analysis. eEJC traces were analyzed for standard parameters (amplitude, rise time, decay, charge flow) with a semi-automatic custom MATLAB script (MathWorks, version R2009a). Stimulation artifacts in eEJC recordings were removed for clarity. mEJC recordings were analyzed with pClamp 10 software (Molecular Devices).

Electron microscopy

Conventional embedding was performed as described previously (Matkovic et al., 2013). In brief, dissected third instar larvae were fixed with PFA (for 10 min in 4% PFA and 0.5% glutaraldehyde in 0.1 M PBS pH 7.4) and glutaraldehyde (for 1 h in 2% glutaraldehyde in 0.1 M sodium cacodylate pH 7.2), washed in 0.1 M sodium cacodylate buffer and postfixed with 1% osmium tetroxide and 0.8% $K_4Fe(CN)_6$ in 0.1 M sodium cacodylate buffer (1 h on ice). After washing with 0.1 M sodium cacodylate buffer and distilled water, the samples were stained with 1% uranyl acetate in distilled water. Samples were dehydrated, infiltrated with Epon resin and then muscle 6/7 of abdominal segment A2/3 was cut out. Collected in an embedding mold, blocks were polymerized and cut in 65-70 nm serial sections. These sections were postfixed and poststained with uranyl acetate/lead citrate. Micrographs were taken with a JEM-1011 electron microscope (JEOL) equipped with an Orius 1200A camera (Gatan) using the DigitalMicrograph software package (Gatan). For quantification, the plasma membrane and the electron-dense T-bar were detected by eye and labeled manually. T-bar roof size was measured by a straight line connecting the furthest distance of the upmost T-bar dense material (in relation to the plasma membrane). Numbers imaged: T-bars, w^{1118} 84, $DAAM^{Ex68}$ 72; boutons, w^{1118} 74, $DAAM^{Ex68}$ 67; animals, w^{1118} 6, $DAAM^{Ex68}$ 6.

Statistics

Data were analyzed with Prism software (GraphPad, version 5). To compare two groups, two-tailed *t*-test or Mann–Whitney *U*-test was used for all data sets. ANOVA was used for multiple comparisons. $P<0.05$ was considered statistically significant. Data are presented as mean±s.e.m. Data distribution was assumed to be normal, but this was not formally tested. No statistical methods were used to predetermine sample sizes, but our sample sizes are similar to those generally employed in the field. Data collection and analyses were not performed blind to the conditions of the experiments, nor was data collection randomized. For STED immunostaining, all genotypes were prepared in one session, stained in one cup and analyzed in an unbiased manner. For electrophysiological recordings, genotypes were measured in an alternating fashion on the same day and strictly analyzed in an unbiased manner.

Acknowledgements

We thank the Bloomington *Drosophila* Stock Center, Developmental Studies Hybridoma Bank (DSHB) at The University of Iowa, Marie-Laure Parmentier, Christian Klämbt, Aaron DiAntonio, Jan Pielage, Christos Samakovlis and Hermann Aberle for fly stocks and reagents; Andor Udvardy and Lajos Pintér for technical advice on affinity purification, and László Sipos for technical advice on generation of the $DAAM^{3xFlag}$ knock-in allele; and Anikó Berente, Edit Gyáni, Ildikó Velkeyné Krausz and Anna Rehák for technical assistance.

Competing interests

The authors declare no competing or financial interests.

Author contributions

Conceptualization: E.M., S. Sigrist, J. Mihály; Methodology: T.G., Z.D., K.F.M.; Investigation: E.M., T.G., I.F., S. Szikora, R.G.; Data curation: E.M., Z.D.; Writing - original draft: E.M., T.G., S. Sigrist, J. Mihály; Writing - review & editing: E.M., I.F., S. Sigrist, J. Mihály; Visualization: E.M., T.G., J. Maléth; Supervision: K.F.M., P.H., S. Sigrist, J. Mihály; Project administration: J. Mihály; Funding acquisition: J. Mihály.

Funding

This work was supported by the Hungarian Science Foundation (Országos Tudományos Kutatási Alapprogramok, OTKA) (K109330 to J. Mihály), the Hungarian Brain Research Program (Nemzeti Agykutatási Program) (KTIA_NAP_13-2-2014-0007 and 2017-1.2.1-NKP-2017-00002 to J. Mihály), the National Research, Development and Innovation Office (Nemzeti Kutatási, Fejlesztési és Innovációs Hivatallal) (GINOP-2.3.2-15-2016-00001 and GINOP-2.3.2-15-2016-00032 to J. Mihály), a Hungarian Academy of Sciences (Magyar Tudományos Akadémia, MTA) Postdoctoral Fellowship (to I.F.) and an OTKA Postdoctoral Fellowship (PD 121193 to R.G.).

Supplementary information

Supplementary information available online at
http://dev.biologists.org/lookup/doi/10.1242/dev.158519.supplemental

References

Aberle, H., Haghighi, A. P., Fetter, R. D., McCabe, B. D., Magalhães, T. R. and Goodman, C. S. (2002). wishful thinking encodes a BMP type II receptor that regulates synaptic growth in Drosophila. *Neuron* **33**, 545-558.

Bartolini, F. and Gundersen, G. G. (2010). Formins and microtubules. *Biochim. Biophys. Acta* **1803**, 164-173.

Bartolini, F., Moseley, J. B., Schmoranzer, J., Cassimeris, L., Goode, B. L. and Gundersen, G. G. (2008). The formin mDia2 stabilizes microtubules independently of its actin nucleation activity. *J. Cell Biol.* **181**, 523-536.

Bosch, M. and Hayashi, Y. (2012). Structural plasticity of dendritic spines. *Curr. Opin. Neurobiol.* **22**, 383-388.

Budnik, V. and Salinas, P. C. (2011). Wnt signaling during synaptic development and plasticity. *Curr. Opin. Neurobiol.* **21**, 151-159.

Bulat, V., Rast, M. and Pielage, J. (2014). Presynaptic CK2 promotes synapse organization and stability by targeting Ankyrin2. *J. Cell Biol.* **204**, 77-94.

Cheng, L., Zhang, J., Ahmad, S., Rozier, L., Yu, H., Deng, H. and Mao, Y. (2011). Aurora B regulates formin mDia3 in achieving metaphase chromosome alignment. *Dev. Cell* **20**, 342-352.

Chesarone, M. A., DuPage, A. G. and Goode, B. L. (2010). Unleashing formins to remodel the actin and microtubule cytoskeletons. *Nat. Rev. Mol. Cell Biol.* **11**, 62-74.

Chia, P. H., Patel, M. R. and Shen, K. (2012). NAB-1 instructs synapse assembly by linking adhesion molecules and F-actin to active zone proteins. *Nat. Neurosci.* **15**, 234-242.

Chia, P. H., Chen, B., Li, P., Rosen, M. K. and Shen, K. (2014). Local F-actin network links synapse formation and axon branching. *Cell* **156**, 208-220.

Cingolani, L. A. and Goda, Y. (2008). Actin in action: the interplay between the actin cytoskeleton and synaptic efficacy. *Nat. Rev. Neurosci.* **9**, 344-356.

Daou, P., Hasan, S., Breitsprecher, D., Baudelet, E., Camoin, L., Audebert, S., Goode, B. L. and Badache, A. (2014). Essential and nonredundant roles for Diaphanous formins in cortical microtubule capture and directed cell migration. *Mol. Biol. Cell* **25**, 658-668.

Fouquet, W., Owald, D., Wichmann, C., Mertel, S., Depner, H., Dyba, M., Hallermann, S., Kittel, R. J., Eimer, S. and Sigrist, S. J. (2009). Maturation of active zone assembly by Drosophila Bruchpilot. *J. Cell Biol.* **186**, 129-145.

Gaillard, J., Ramabhadran, V., Neumanne, E., Gurel, P., Blanchoin, L., Vantard, M. and Higgs, H. N. (2011). Differential interactions of the formins INF2, mDia1, and mDia2 with microtubules. *Mol. Biol. Cell* **22**, 4575-4587.

Goellner, B. and Aberle, H. (2012). The synaptic cytoskeleton in development and disease. *Dev. Neurobiol.* **72**, 111-125.
Gögel, S., Wakefield, S., Tear, G., Klämbt, C. and Gordon-Weeks, P. R. (2006). The Drosophila microtubule associated protein Futsch is phosphorylated by Shaggy/Zeste-white 3 at an homologous GSK3beta phosphorylation site in MAP1B. *Mol. Cell. Neurosci.* **33**, 188-199.
Gombos, R., Migh, E., Antal, O., Mukherjee, A., Jenny, A. and Mihaly, J. (2015). The formin DAAM functions as molecular effector of the planar cell polarity pathway during axonal development in Drosophila. *J. Neurosci.* **35**, 10154-10167.
Gratz, S. J., Cummings, A. M., Nguyen, J. N., Hamm, D. C., Donohue, L. K., Harrison, M. M., Wildonger, J. and O'Connor-Giles, K. M. (2013). Genome engineering of Drosophila with the CRISPR RNA-guided Cas9 nuclease. *Genetics* **194**, 1029-1035.
Guan, S., Price, J. C., Prusiner, S. B., Ghaemmaghami, S. and Burlingame, A. L. (2011). A data processing pipeline for mammalian proteome dynamics studies using stable isotope metabolic labeling. *Mol. Cell. Proteomics* **10**, M111 010728.
Habas, R., Kato, Y. and He, X. (2001). Wnt/Frizzled activation of Rho regulates vertebrate gastrulation and requires a novel Formin homology protein Daam1. *Cell* **107**, 843-854.
Henty-Ridilla, J. L., Rankova, A., Eskin, J. A., Kenny, K. and Goode, B. L. (2016). Accelerated actin filament polymerization from microtubule plus ends. *Science* **352**, 1004-1009.
Hirokawa, N., Sobue, K., Kanda, K., Harada, A. and Yorifuji, H. (1989). The cytoskeletal architecture of the presynaptic terminal and molecular structure of synapsin 1. *J. Cell Biol.* **108**, 111-126.
Hummel, T., Krukkert, K., Roos, J., Davis, G. and Klämbt, C. (2000). Drosophila Futsch/22C10 is a MAP1B-like protein required for dendritic and axonal development. *Neuron* **26**, 357-370.
Kevenaar, J. T. and Hoogenraad, C. C. (2015). The axonal cytoskeleton: from organization to function. *Front. Mol. Neurosci.* **8**, 44.
Kim, S., Ko, J., Shin, H., Lee, J.-R., Lim, C., Han, J.-H., Altrock, W. D., Garner, C. C., Gundelfinger, E. D., Premont, R. T. et al. (2003). The GIT family of proteins forms multimers and associates with the presynaptic cytomatrix protein Piccolo. *J. Biol. Chem.* **278**, 6291-6300.
Kittel, R. J., Wichmann, C., Rasse, T. M., Fouquet, W., Schmidt, M., Schmid, A., Wagh, D. A., Pawlu, C., Kellner, R. R., Willig, K. I. et al. (2006). Bruchpilot promotes active zone assembly, Ca2+ channel clustering, and vesicle release. *Science* **312**, 1051-1054.
Koch, I., Schwarz, H., Beuchle, D., Goellner, B., Langegger, M. and Aberle, H. (2008). Drosophila ankyrin 2 is required for synaptic stability. *Neuron* **58**, 210-222.
Koch, N., Kobler, O., Thomas, U., Qualmann, B. and Kessels, M. M. (2014). Terminal axonal arborization and synaptic bouton formation critically rely on abp1 and the arp2/3 complex. *PLoS ONE* **9**, e97692.
Lee, H. K. and Deneen, B. (2012). Daam2 is required for dorsal patterning via modulation of canonical Wnt signaling in the developing spinal cord. *Dev. Cell* **22**, 183-196.
Lepicard, S., Franco, B., de Bock, F. and Parmentier, M.-L. (2014). A presynaptic role of microtubule-associated protein 1/Futsch in Drosophila: regulation of active zone number and neurotransmitter release. *J. Neurosci.* **34**, 6759-6771.
Lewkowicz, E., Herit, F., Le Clainche, C., Bourdoncle, P., Perez, F. and Niedergang, F. (2008). The microtubule-binding protein CLIP-170 coordinates mDia1 and actin reorganization during CR3-mediated phagocytosis. *J. Cell Biol.* **183**, 1287-1298.
Li, Y.-C., Bai, W.-Z., Zhou, L., Sun, L.-K. and Hashikawa, T. (2010). Nonhomogeneous distribution of filamentous actin in the presynaptic terminals on the spinal motoneurons. *J. Comp. Neurol.* **518**, 3184-3192.
Luchtenborg, A.-M., Solis, G. P., Egger-Adam, D., Koval, A., Lin, C., Blanchard, M. G., Kellenberger, S. and Katanaev, V. L. (2014). Heterotrimeric Go protein links Wnt-Frizzled signaling with ankyrins to regulate the neuronal microtubule cytoskeleton. *Development* **141**, 3399-3409.
Marrus, S. B., Portman, S. L., Allen, M. J., Moffat, K. G. and DiAntonio, A. (2004). Differential localization of glutamate receptor subunits at the Drosophila neuromuscular junction. *J. Neurosci.* **24**, 1406-1415.
Matkovic, T., Siebert, M., Knoche, E., Depner, H., Mertel, S., Owald, D., Schmidt, M., Thomas, U., Sickmann, A., Kamin, D. et al. (2013). The Bruchpilot cytomatrix determines the size of the readily releasable pool of synaptic vesicles. *J. Cell Biol.* **202**, 667-683.
Matusek, T., Djiane, A., Jankovics, F., Brunner, D., Mlodzik, M. and Mihaly, J. (2006). The Drosophila formin DAAM regulates the tracheal cuticle pattern through organizing the actin cytoskeleton. *Development* **133**, 957-966.
Matusek, T., Gombos, R., Szecsenyi, A., Sanchez-Soriano, N., Czibula, A., Pataki, C., Gedai, A., Prokop, A., Rasko, I. and Mihaly, J. (2008). Formin proteins of the DAAM subfamily play a role during axon growth. *J. Neurosci.* **28**, 13310-13319.
McCabe, B. D., Hom, S., Aberle, H., Fetter, R. D., Marques, G., Haerry, T. E., Wan, H., O'Connor, M. B., Goodman, C. S. and Haghighi, A. P. (2004). Highwire regulates presynaptic BMP signaling essential for synaptic growth. *Neuron* **41**, 891-905.
Miech, C., Pauer, H.-U., He, X. and Schwarz, T. L. (2008). Presynaptic local signaling by a canonical wingless pathway regulates development of the Drosophila neuromuscular junction. *J. Neurosci.* **28**, 10875-10884.
Molnar, I., Migh, E., Szikora, S., Kalmár, T., Végh, A. G., Deak, F., Barko, S., Bugyi, B., Orfanos, Z., Kovács, J. et al. (2014). DAAM is required for thin filament formation and Sarcomerogenesis during muscle development in Drosophila. *PLoS Genet.* **10**, e1004166.
Morales, M., Colicos, M. A. and Goda, Y. (2000). Actin-dependent regulation of neurotransmitter release at central synapses. *Neuron* **27**, 539-550.
Nelson, J. C., Stavoe, A. K. and Colón-Ramos, D. A. (2013). The actin cytoskeleton in presynaptic assembly. *Cell Adhes. Migration* **7**, 379-387.
Owald, D., Fouquet, W., Schmidt, M., Wichmann, C., Mertel, S., Depner, H., Christiansen, F., Zube, C., Quentin, C., Körner, J. et al. (2010). A Syd-1 homologue regulates pre- and postsynaptic maturation in Drosophila. *J. Cell Biol.* **188**, 565-579.
Packard, M., Koo, E. S., Gorczyca, M., Sharpe, J., Cumberledge, S. and Budnik, V. (2002). The Drosophila Wnt, wingless, provides an essential signal for pre- and postsynaptic differentiation. *Cell* **111**, 319-330.
Pawson, C., Eaton, B. A. and Davis, G. W. (2008). Formin-dependent synaptic growth: evidence that Dlar signals via Diaphanous to modulate synaptic actin and dynamic pioneer microtubules. *J. Neurosci.* **28**, 11111-11123.
Phillips, G. R., Huang, J. K., Wang, Y., Tanaka, H., Shapiro, L., Zhang, W., Shan, W.-S., Arndt, K., Frank, M., Gordon, R. E. et al. (2001). The presynaptic particle web: ultrastructure, composition, dissolution, and reconstitution. *Neuron* **32**, 63-77.
Pielage, J., Fetter, R. D. and Davis, G. W. (2005). Presynaptic spectrin is essential for synapse stabilization. *Curr. Biol.* **15**, 918-928.
Pielage, J., Cheng, L., Fetter, R. D., Carlton, P. M., Sedat, J. W. and Davis, G. W. (2008). A presynaptic giant ankyrin stabilizes the NMJ through regulation of presynaptic microtubules and transsynaptic cell adhesion. *Neuron* **58**, 195-209.
Qin, G., Schwarz, T., Kittel, R. J., Schmid, A., Rasse, T. M., Kappei, D., Ponimaskin, E., Heckmann, M. and Sigrist, S. J. (2005). Four different subunits are essential for expressing the synaptic glutamate receptor at neuromuscular junctions of Drosophila. *J. Neurosci.* **25**, 3209-3218.
Roos, J., Hummel, T., Ng, N., Klämbt, C. and Davis, G. W. (2000). Drosophila Futsch regulates synaptic microtubule organization and is necessary for synaptic growth. *Neuron* **26**, 371-382.
Rosales-Nieves, A. E., Johndrow, J. E., Keller, L. C., Magie, C. R., Pinto-Santini, D. M. and Parkhurst, S. M. (2006). Coordination of microtubule and microfilament dynamics by Drosophila Rho1, Spire and Cappuccino. *Nat. Cell Biol.* **8**, 367-376.
Stephan, R., Goellner, B., Moreno, E., Frank, C. A., Hugenschmidt, T., Genoud, C., Aberle, H. and Pielage, J. (2015). Hierarchical microtubule organization controls axon caliber and transport and determines synaptic structure and stability. *Dev. Cell* **33**, 5-21.
Sugie, A., Hakeda-Suzuki, S., Suzuki, E., Silies, M., Shimozono, M., Möhl, C., Suzuki, T. and Tavosanis, G. (2015). Molecular remodeling of the presynaptic active zone of Drosophila photoreceptors via activity-dependent feedback. *Neuron* **86**, 711-725.
Szikora, S., Földi, I., Tóth, K., Migh, E., Vig, A., Bugyi, B., Maleth, J., Hegyi, P., Kaltenecker, P., Sanchez-Soriano, N. et al. (2017). The formin DAAM is required for coordination of the actin and microtubule cytoskeleton in axonal growth cones. *J. Cell Sci.* **130**, 2506-2519.
Vig, A. T., Földi, I., Szikora, S., Migh, E., Gombos, R., Tóth, M. Á., Huber, T., Pintér, R., Talián, G. C., Mihály, J. et al. (2017). The activities of the C-terminal regions of the formin protein disheveled-associated activator of morphogenesis (DAAM) in actin dynamics. *J. Biol. Chem.* **292**, 13566-13583.
Wagh, D., Terry-Lorenzo, R., Waites, C. L., Leal-Ortiz, S. A., Maas, C., Reimer, R. J. and Garner, C. C. (2015). Piccolo directs activity dependent F-actin assembly from presynaptic active zones via Daam1. *PLoS ONE* **10**, e0120093.
Waites, C. L., Leal-Ortiz, S. A., Andlauer, T. F. M., Sigrist, S. J. and Garner, C. C. (2011). Piccolo regulates the dynamic assembly of presynaptic F-actin. *J. Neurosci.* **31**, 14250-14263.
Wallar, B. J. and Alberts, A. S. (2003). The formins: active scaffolds that remodel the cytoskeleton. *Trends Cell Biol.* **13**, 435-446.
Wang, X., Kibschull, M., Laue, M. M., Lichte, B., Petrasch-Parwez, E. and Kilimann, M. W. (1999). Aczonin, a 550-kD putative scaffolding protein of presynaptic active zones, shares homology regions with Rim and Bassoon and binds profilin. *J. Cell Biol.* **147**, 151-162.
Wen, Y., Eng, C. H., Schmoranzer, J., Cabrera-Poch, N., Morris, E. J. S., Chen, M., Wallar, B. J., Alberts, A. S. and Gundersen, G. G. (2004). EB1 and APC bind to mDia to stabilize microtubules downstream of Rho and promote cell migration. *Nat. Cell Biol.* **6**, 820-830.
Young, K. G. and Copeland, J. W. (2010). Formins in cell signaling. *Biochim. Biophys. Acta* **1803**, 183-190.

Supplementary Figures

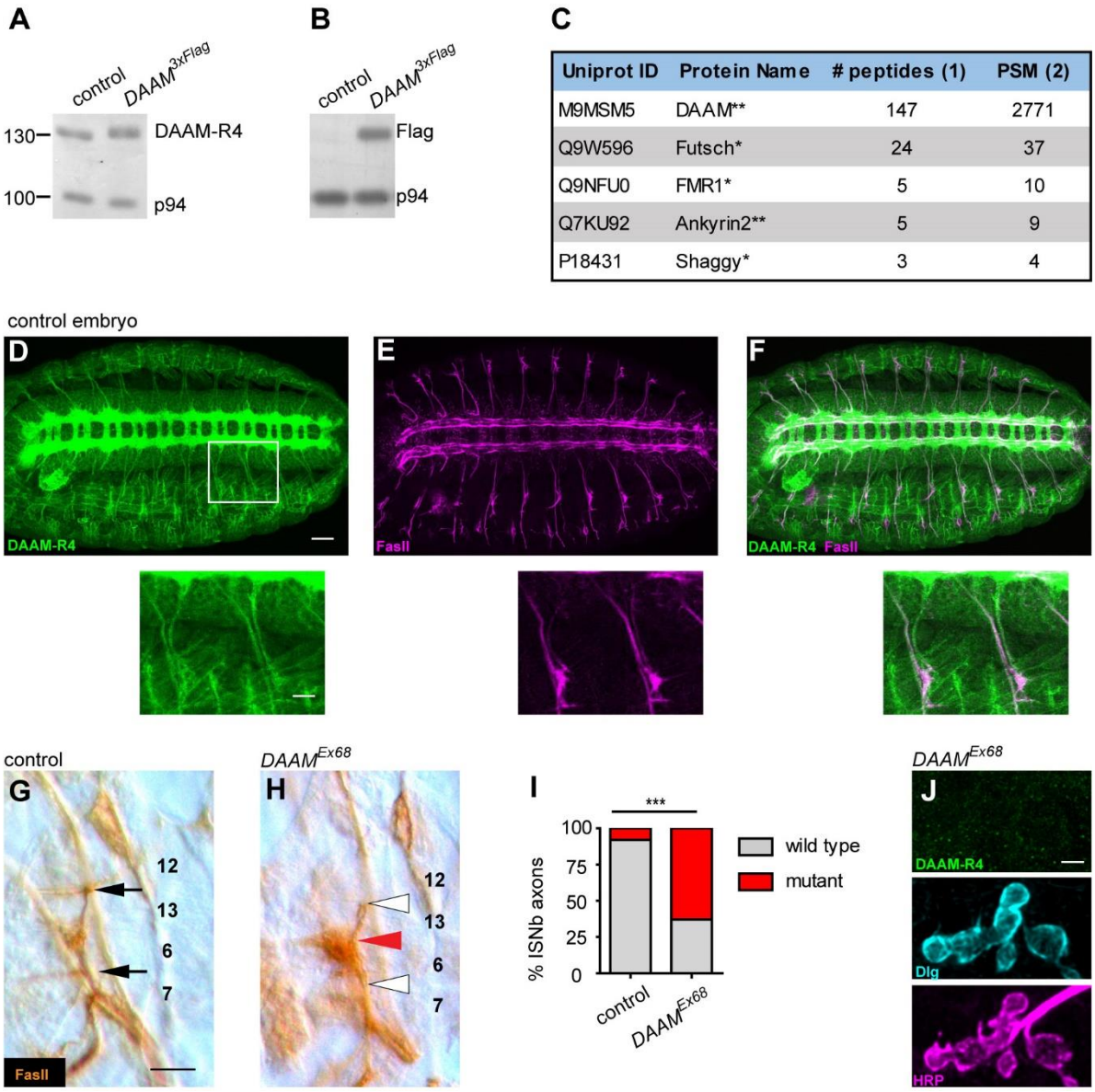

Uniprot ID	Protein Name	# peptides (1)	PSM (2)
M9MSM5	DAAM**	147	2771
Q9W596	Futsch*	24	37
Q9NFU0	FMR1*	5	10
Q7KU92	Ankyrin2**	5	9
P18431	Shaggy*	3	4

Figure S1. MS analysis of the DAAM::Flag containing protein complexes and the role of DAAM during embryonic NMJ development.

(**A**-**B**) Western blot analysis of a *DAAM*^{3xFlag} knock-in allele, the anti-p94 (glycogen phosphorylase) antibody was used as a loading control. (**A**) An anti-DAAM-R4 western blot from adult heads revealed that the DAAM::3xFlag protein level is nearly identical to wild type DAAM levels. (**B**) An anti-Flag western blot from adult heads indicates that the DAAM::3xFlag protein is indeed only expressed in *DAAM*^{3xFlag} but not in control (w^{1118}) flies.

(**C**) After purification of the DAAM::3xFlag containing protein complexes, MS analysis identified several proteins as potential DAAM interaction partners which are well known to play a role in synaptogenesis. * indicates proteins unique to the DAAM-Flag sample, ** indicates where protein concentration was found to be at least 2-fold higher as compared to control sample (estimated by spectral counting). (1) shows the number of unique peptide identifications, while PSM (2) indicates the total number of identified peptide spectra matched for a given protein. (**D-F**) Embryonic expression pattern of DAAM in stage 15 control (w^{1118}) embryos as revealed by anti-DAAM-R4 staining (**D, F**). DAAM strongly colocalizes with the motorneuron specific FasII protein (**E, F**) including the axon terminal regions **(**enlarged on the panels below D-F). (**G**) In wild type embryos the FasII positive ISNb axons are known to find their target sites and form synaptic connections with muscles 12-13 and 6-7 (black arrows). In contrast to this, in $DAAM^{Ex68}$ mutant embryos (**H**) terminals of the ISNb nerves often showed guidance defects with premature terminations (white arrows) (**H)** quantified in **(I**). Moreover, the ISNb axons displayed growth phenotypes indicated by strong FasII accumulations (red arrow in H). (**J**) Specificity of the anti-DAAM-R4 antibody is demonstrated by staining of $DAAM^{Ex68}$ mutant NMJs where the level of DAAM is strongly reduced without affecting the Dlg and HRP patterns. Scale bar, 20 µm (**D-H**), 10 µm (**D-F** high magnification pictures) 2 µm (**J**). *** $p<0.001$. $n\geq100$ (**I**).

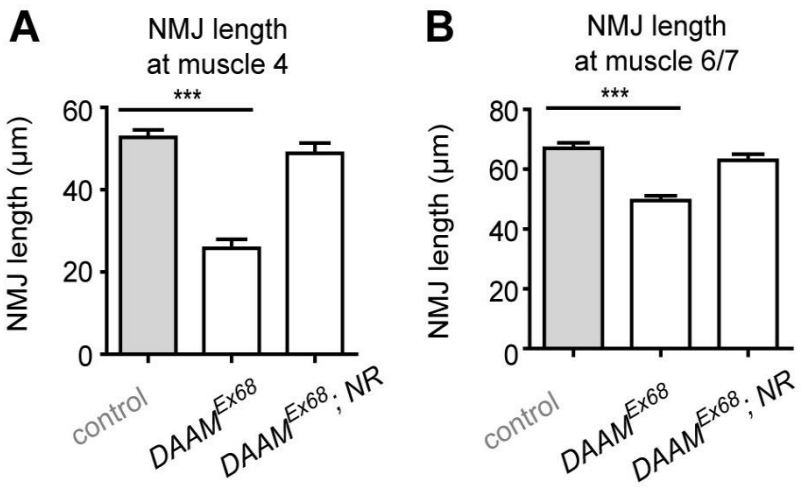

Figure S2. Quantification of NMJ length and bouton number in *DAAM* mutant NMJs.
(**A-B**) Quantification of NMJ length at muscle 4 and 6/7 in control (w^{1118}), $DAAM^{Ex68}$ and $DAAM^{Ex68}$*; NR* ($DAAM^{Ex68;}$*UAS-FLDAAM/+; D42-Gal4/+*) L2 larvae. Error bars indicate s.e.m. *** $p<0.001$. $n\geq25$ (**A, B**).

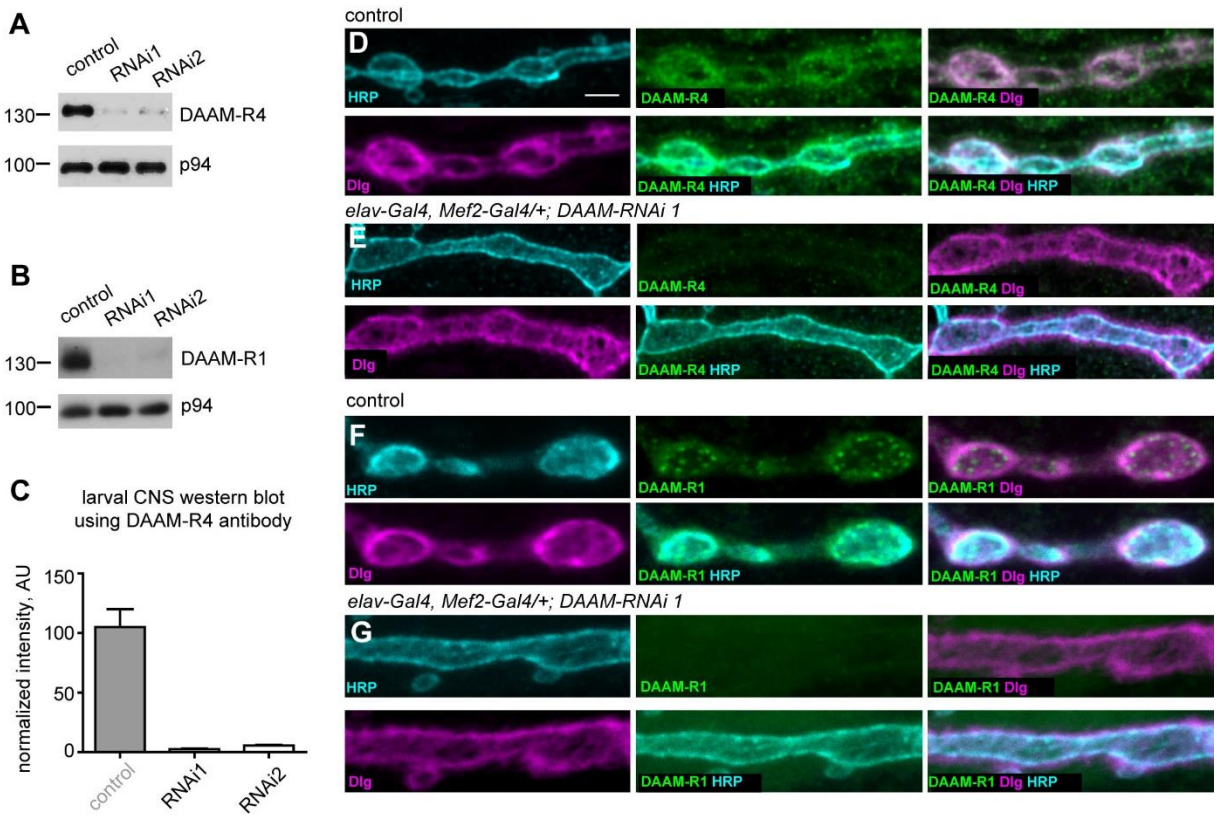

Figure S3. Knock-down effect of the *DAAM* RNAi lines.

Western blots show that the two *DAAM* specific RNAi lines are very effectively knocking-down the *DAAM* gene that is demonstrated by the R4 (**A**) and R1 (**B**) antibodies as well, quantification is provided for the R4 blot in panel **C**. Whereas in w^{1118} control NMJs (**D**) DAAM displays a cortical accumulation as detected by R4, upon pre- and postsynaptic knock-down of DAAM by RNAi1, the DAAM signal can barely detected in the NMJs with R4 (**E**). The R1 antibody labels a largely punctual pattern within control NMJs (**F**), and similarly to the case of R4, this staining is virtually absent when DAAM is knocked-down by RNAi (**G**). To visualize the NMJ terminals, anti-Dlg (green) and anti-HRP (magenta) synaptic markers were used. Scale bar, 3 μm (**D-G**).

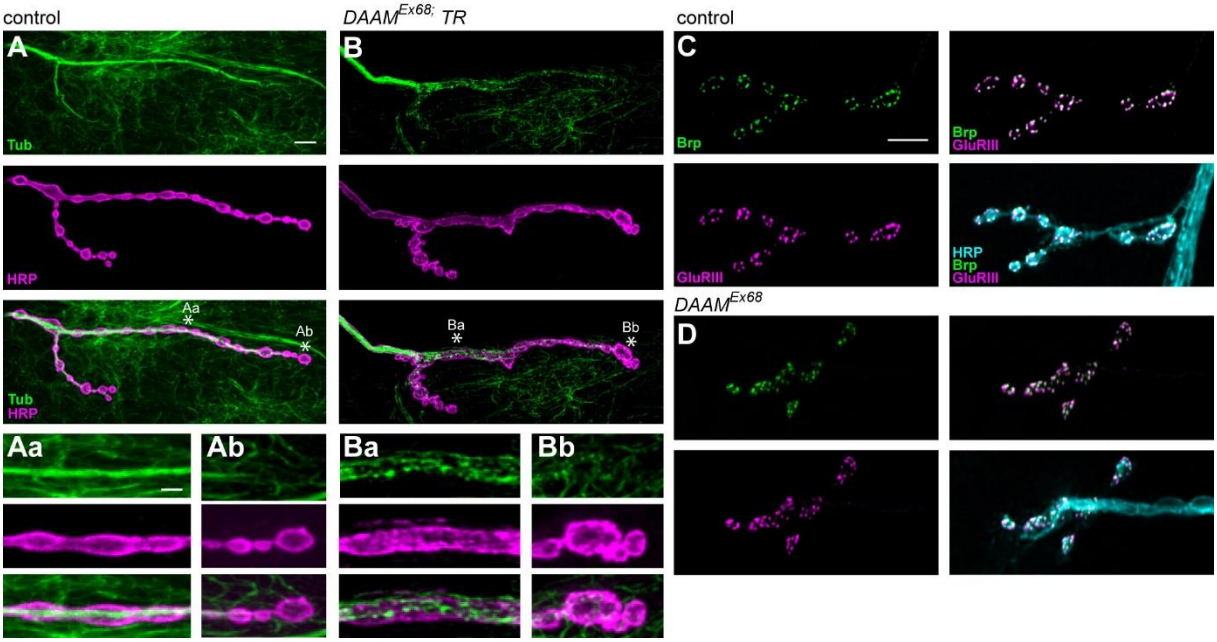

Figure S4. Lack of *DAAM* leads to MT fragmentation but not to synaptic instability

(A-B) Analysis of MT organization at muscle 4 NMJs in control (w^{1118}) (**A**) and $DAAM^{Ex68}$; *TR* (**B**) animals using anti-Tubulin (green) and HRP (magenta) markers. (**Aa, Ab, Ba, Bb**) High magnification pictures show the central (**Aa, Ba**) and terminal region (**Ab, Bb**) of the NMJs shown in panel A and B. (**C-D**) Similar to w^{1118} controls (**C**), $DAAM^{Ex68}$ mutant NMJs (**D**) do not show signs of synaptic retractions as judged by anti-Brp (green) and anti-GluRIII (magenta) double staining. Scale bar, 5 µm (**A, B, C, D**), 2 µm (**Aa, Ab, Ba, Bb)**.

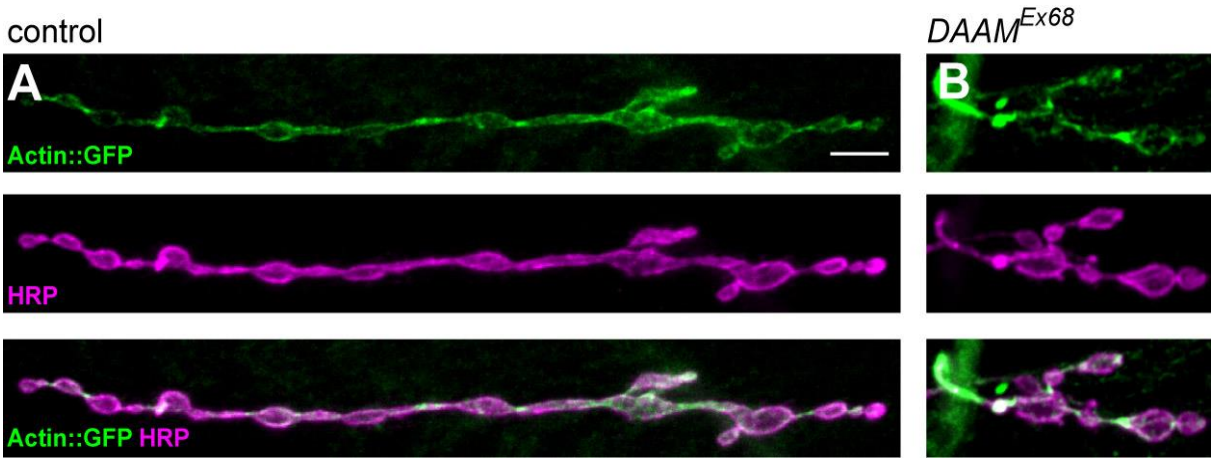

Figure S5. The absence of DAAM does not affect actin organization within the NMJs.

Confocal images show organization of the actin cytoskeleton (detected by Actin::GFP, in green) in w^{1118} control (**A**) and in $DAAM^{Ex68}$ mutant NMJs (**B**), outlined by HRP (in magenta) staining. The subcortical actin staining is evident in both cases, while overt alterations in the pattern are not obvious (at least, at this level of resolution) when *DAAM* is compared to controls. Note the difference in NMJ length which is much shorter in the mutant situation. Scale bar, 5 μm (**A**-**B**).

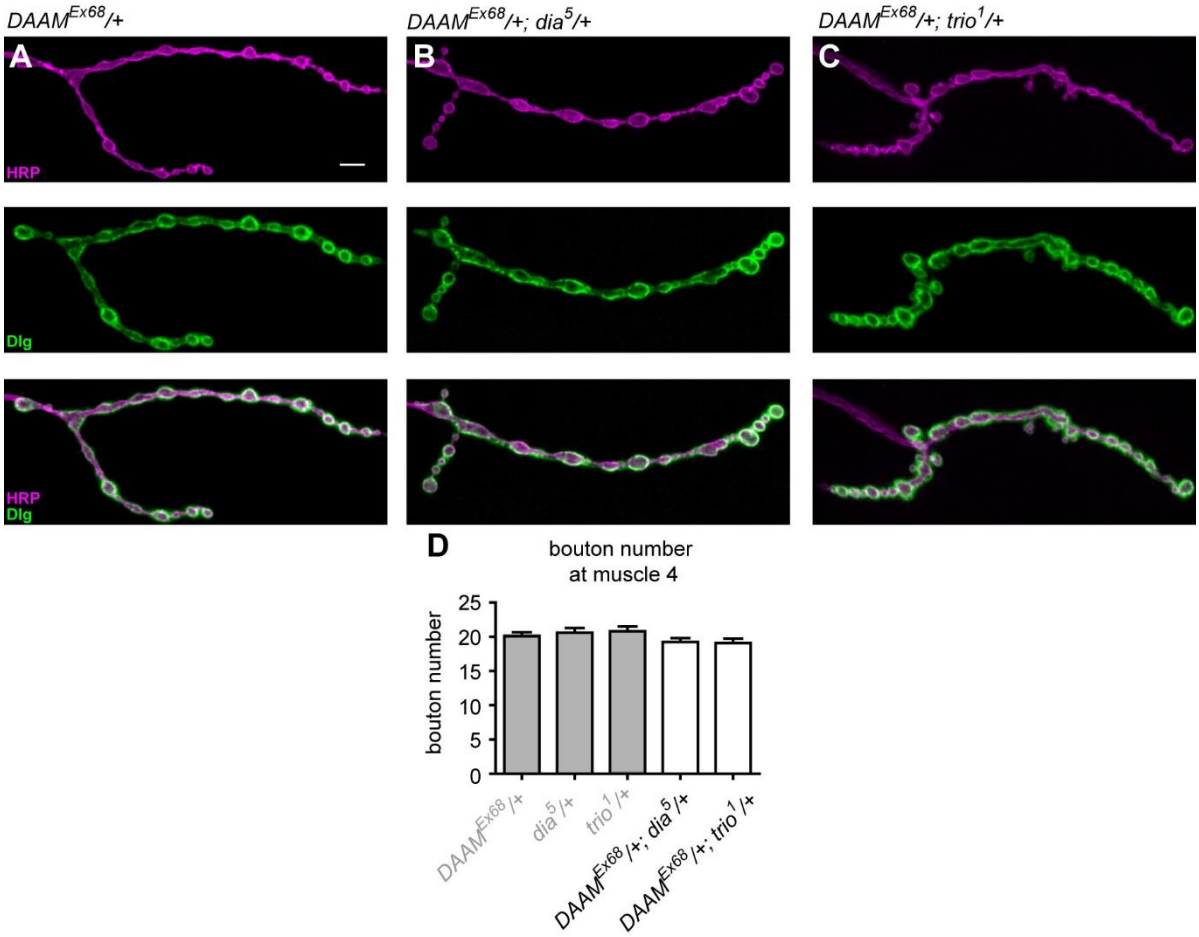

Figure S6. Mutations affecting *dia* or *trio* do not exhibit a genetic interaction with that of *DAAM* in transheterozygous conditions.

NMJs of heterozygous mutant L3 larvae of the genotypes indicated (**A-C**), stained with anti-HRP (in magenta) and Dlg (in green). (**D**) Quantification of the bouton numbers observed in larvae shown in panels A-C and in dia^5/+ and $trio^1$/+ controls. Note that presence of a *dia* (**B**) or *trio* (**C**) mutation in a heterozygous $DAAM^{Ex68}$ background (**A**) does not alter bouton number (quantified in **D**) or NMJ morphology. Scale bar, 5 µm (**A-B**). Error bars indicate s.e.m. n≥25 (**D**).

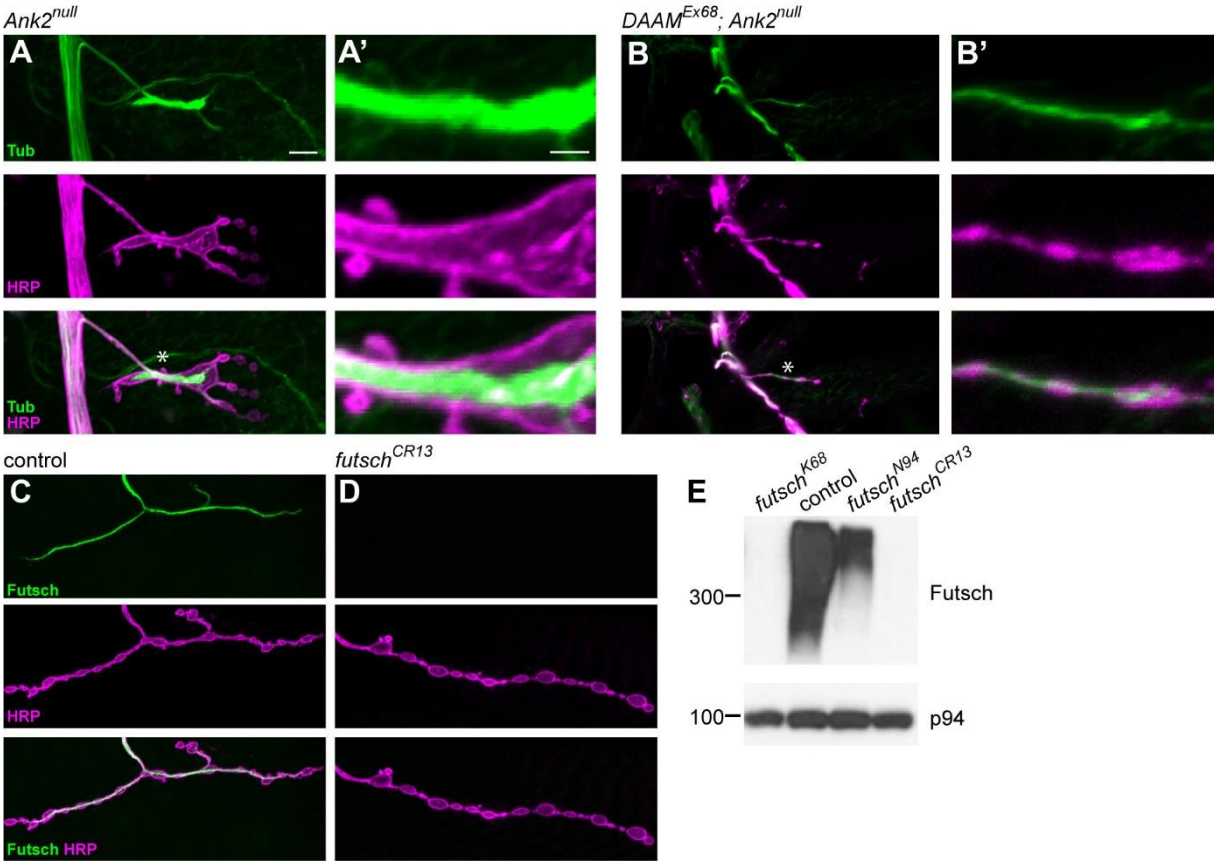

Figure S7. Epistatic analysis of *DAAM* with *Ank2*^{null} and characterization of the new *futsch* CRISPR null allele

(**A-B'**) Analysis of MT organization at muscle 4 NMJs in *Ank2*^{null} (**A, A'**) and *DAAM*^{Ex68}; *Ank2*^{null} (**B, B'**) mutant larvae visualized by anti-Tubulin (green) and anti-HRP (magenta) staining. (**A', B')** High magnification images of the central region of the NMJs indicated by asterisk in A and B. The bouton fusion and MT accumulation phenotype of *Ank2*^{null} (**A, A'**) is suppressed by *DAAM*^{Ex68} (**B**, **B'**). Whereas we can detect a strong Futsch accumulation in *w*^{1118} control NMJs (**C**), no Futsch signal can be detected in NMJs of the newly isolated *futsch*^{CR13} allele (**D**). (**E**) In line with the immunostaining experiments, Western blot analysis clearly indicates that the 22C10 antibody fails to detect the presence of the Futsch protein in *futsch*^{CR13} which is similar to the case of *futsch*^{K68} a previously isolated protein null allele. Anti-p94 (glycogen phosphorylase) antibody was used as a loading control. Scale bar, 5 μm (**A, B, C, D**), 2 μm (**A', B'**).

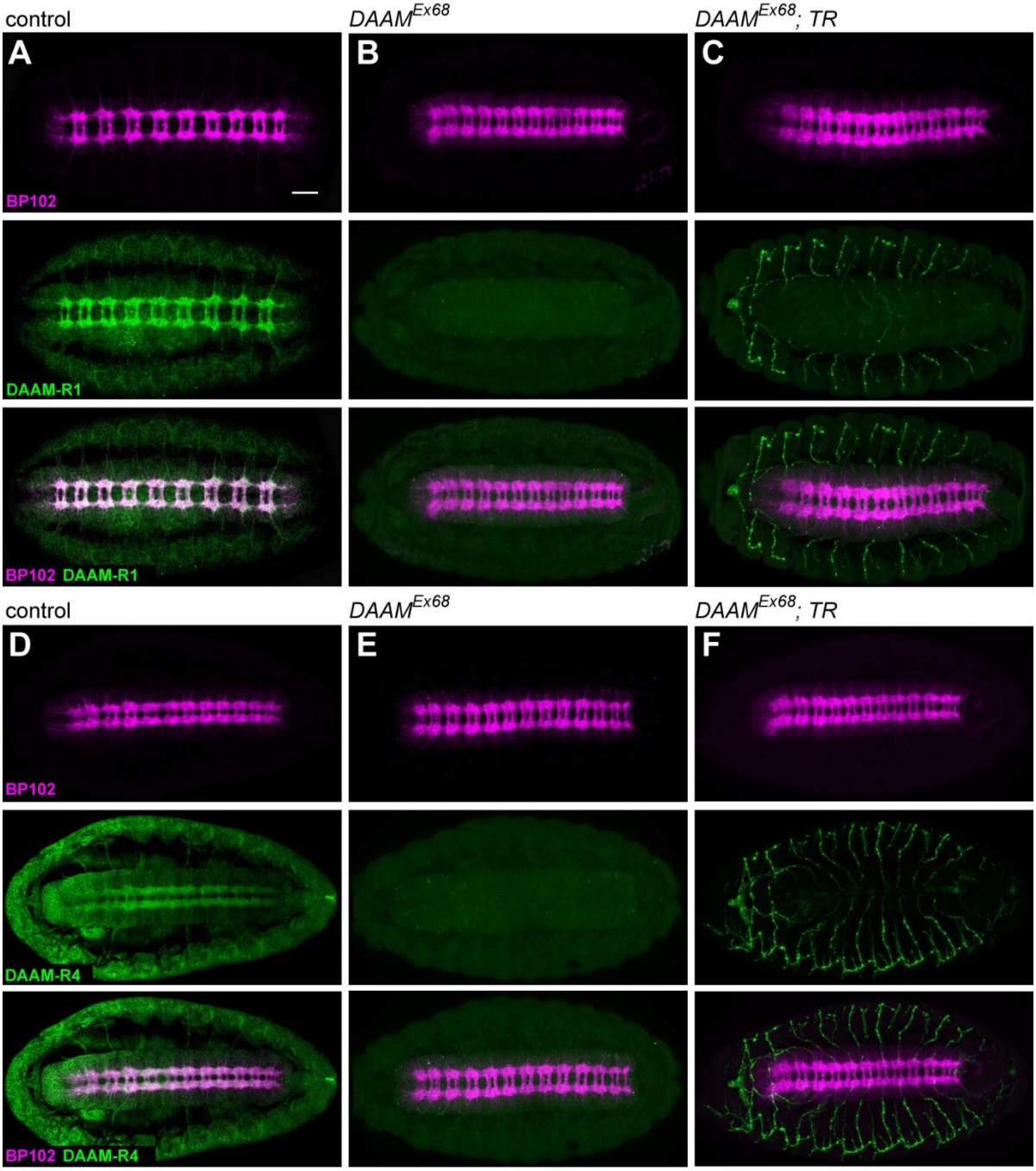

Figure S8. Comparison of the staining pattern of two DAAM antibodies in the embryonic CNS.

(**A**-**F**) Confocal images (ventral views) are shown from stage 15 embryos to compare the staining pattern of the R1 and R4 antibodies within the ventral nerve cord (VNC). In w^{1118} control embryos the R1 (**A**) and R4 (**D**) antibodies (in green) label the VNC highly specifically. Note that the DAAM pattern strongly overlaps with that of the axonal marker BP102 (in magenta). In $DAAM^{Ex68}$ zygotically null mutant embryos the R1 and R4 staining is

nearly entirely absent (only a weak background staining can be detected) (**B, E**), while the BP102 pattern remains unaffected. As expected, when FL-DAAM is expressed exclusively in the tracheal system in a $DAAM^{Ex68}$ mutant background ($DAAM^{Ex68}$; *TR*), R1 (**C**) and R4 (**F**) are both able to detect a strong DAAM signal in the tracheal system but no staining is evident within the VNC including the BP102 positive axons. Scale bar, 20 µm (**A-F**).

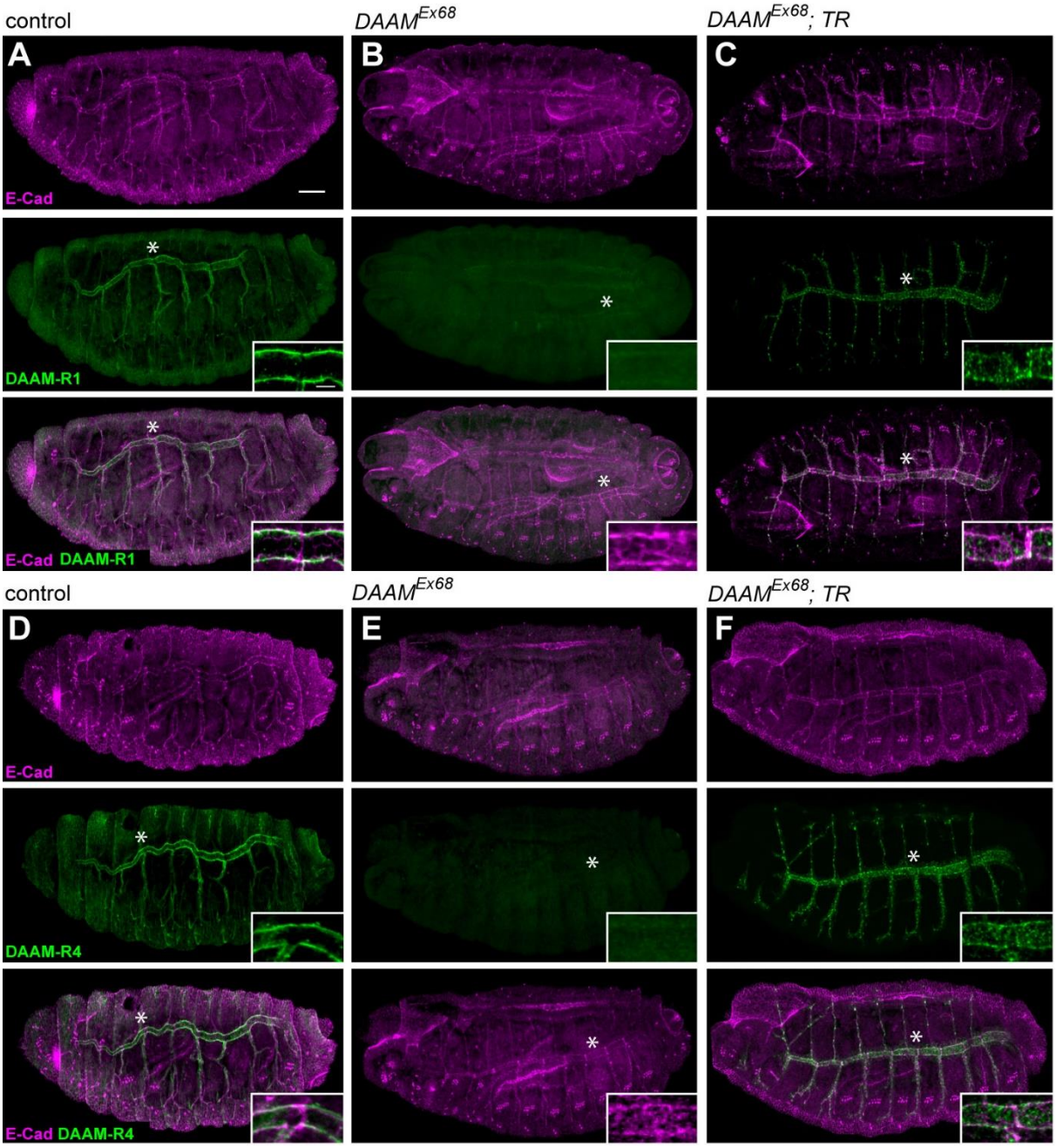

Figure S9. Comparison of the staining pattern of two DAAM antibodies in the embryonic tracheal system.

We compared the tracheal expression pattern of the R1 and R4 anti-DAAM serum within stage 16 embryos by confocal imaging. In w^{1118} control embryos the R1 (**A**) and R4 (**D**) antibodies label the tracheal system highly specifically. The staining pattern appears as a largely subcortical pattern as shown on the insets in the bottom right corner of the panels (asterisks indicate the dorsal trunk region shown on the insets). Drosophila E-Cad (in magenta) was used to outline the embryonic cell borders, whereas the green channel was used

to visualize the DAAM protein either with R1 (**A-C**) or R4 (**D-F**). In *DAAM*^{Ex68} zygotically null mutant embryos the R1 and R4 staining is nearly entirely absent (**B, E**), while the E-Cad pattern remains unaffected. As expected, when FL-DAAM is expressed exclusively in the tracheal system in a *DAAM*^{Ex68} mutant background (*DAAM*^{Ex68}; *TR*), R1 (**C**) and R4 (**F**) are both able to detect a strong DAAM signal in tracheal cells. Note that in this condition DAAM often seems to enrich in protein aggregates (presumably due to the elevated expression level) (insets in the bottom right corner) that is not identical to the wild type pattern, nevertheless, the R1 and R4 antibodies are both clearly able to specifically recognize the endogenous as well as the overexpressed DAAM protein in the tracheal system. Scale bar, 20 μm (**A-F**), 5 μm (**A-F** high magnification pictures).

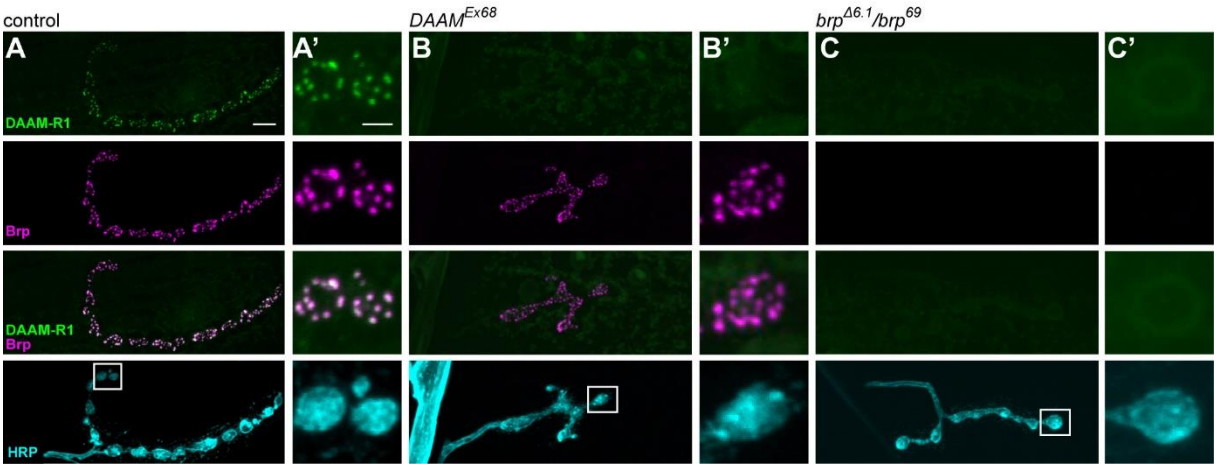

Figure S10. DAAM protein localization at the synaptic AZs.

(**A-C**) Analysis of DAAM localization at muscle 4 NMJs in control (w^{1118}) (**A, A'**), $DAAM^{Ex68}$ (**B, B'**) and *brp* null mutant ($brp^{\Delta 6.1}/brp^{69}$) (**C, C'**) animals using anti-DAAM-R1 (green), anti-Brp (magenta) and anti-HRP (cyan) antibodies. Note that DAAM accumulation is lost in both mutant situations. White squares in A, B and C indicate the regions shown with high magnification in A', B' and C', respectively. Scale bar, 5 µm (**A, B, C**), 2 µm (**A', B', C'**).

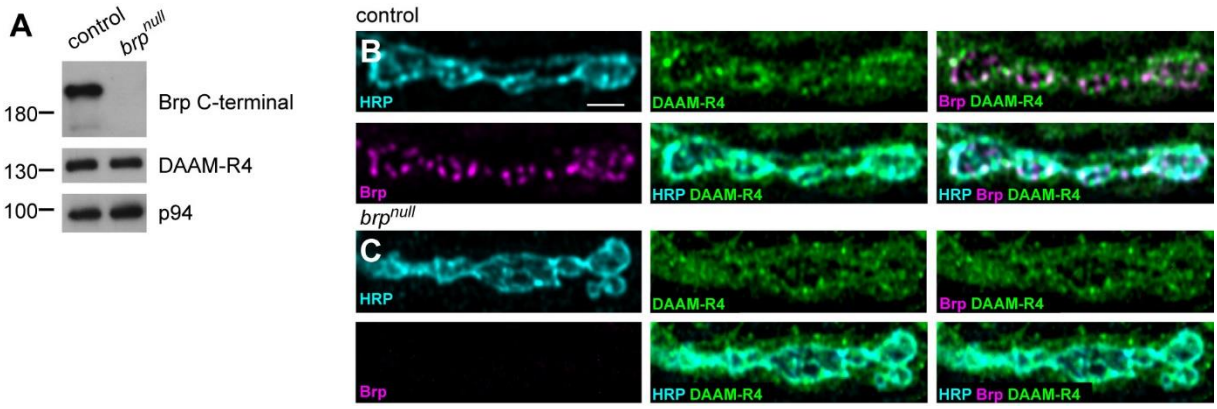

Figure S11. Brp is not required for DAAM stability and cortical accumulation in nerve terminals.

(**A)** A Western blot is shown to demonstrate that in a *brp* null mutant larval brain the DAAM protein is expressed at the same level as in wild type controls. (**B-C**) DAAM staining with the R4 antibody in w^{1118} control NMJs (**B**) displays an accumulation in the cortical membrane area that can still be detected in *brp* mutant (**C**) NMJs. Note that the Brp (in magenta) and DAAM-R4 (in green) patterns are only partly overlapping in the control NMJ (upper right panel). Scale bar, 3 μm (**B-C**).

Supplementary Table 1. List of primer sequences used in this study.

Primer name	Sequence	Purpose
DAAM-732-F	CACCGCTCTGCTGAGCAAACTG	*UAS-FLDAAM*^{732}
DAAM-732-R	CAGTTCTGCGCCCGACGTCC	*UAS-FLDAAM*^{732}
DAAM-876-881-F	GACACCGCGTCCAGTGCCG	*UAS-FLDAAM*$^{876-881}$
DAAM-876-881-R	CGCCAGCGCGTTGAGTGAC	*UAS-FLDAAM*$^{876-881}$
DAAMFH2-shRNA-F	CTAGCAGTGAGCGACATGGAGAT ATCAAATAGTTATATTCAAGCATA TTTGATATCTCCATGTCGCTCGCG	*UAS-shRNA-DAAMFH2*
DAAMFH2-shRNA-R	AATTCGCGAGCGACATGGAGATA TCAAATATGCTTGAATATAACTAT TTGATATCTCCATGTCGCTCACTG	*UAS-shRNA-DAAMFH2*
pCFD4-Futsch-1F	TATATAGGAAAGATATCCGGGTG AACTTCGCAGCTGGCCCAGTTCCT GAGTTTTAGAGCTAGAAATAGCA AG	*futsch*^{CR13}, *DAAM*^{Ex68}, *futsch*^{CR13}
pCFD4-Futsch-3R	ATTTTAACTTGCTATTTCTAGCTCT AAAACGCCCGCTCACCGGCTGCTA CGACGTTAAATTGAAAATAGGTC	*futsch*^{CR13}, *DAAM*^{Ex68}, *futsch*^{CR13}

Supplementary Materials and Methods

In-gel digestion protocol

Gel slices were cut into small (~1 mm^2) pieces, transferred to low-bind 0.5 ml Eppendorf tubes then washed with 3x 50 µl 25 mM ammonium bicarbonate (ABC) / 50 % acetonitrile (ACN). Protein disulfide bridges were reduced by incubating with 20 µl of 10 mM dithiotreithol / 25 mM ABC at 56 ˚C for 30 min then the resulting free sulfhydryl groups were capped by incubating with 25 µl of 55 mM iodoacetamide / 25 mM ABC for 30 min at room temperature (RT) in the dark. The gel pieces were washed with 2x 50 µl 25 mM ABC / 50% ACN then dried down in a vacuum centrifuge. The gel pieces were rehydrated for 10 min at 4 ˚C with 20 µl 5 ng/µl trypsin (Promega V511A) / 25 mM ABC, then additional 25 mM ABC was added to cover the gel pieces. The samples were incubated at 37 ˚C for 4 h. Tryptic peptides were extracted from the gel by vortexing (20 min at RT) then sonicating (5 min at RT) with 2x 50 µl 2% formic acid / 50% ACN. The digest solutions were dried down in a vacuum centrifuge then dissolved in 15 µl 0.1% formic acid and subjected to LC-MS/MS analyses.